SYNTHESIS AND CHARACTERIZATION OF MAGNESIUM-SILICON AND MAGNESIUM-TIN SOLID SOLUTIONS FOR THERMOELECTRIC APPLICATIONS

A Thesis

by

FANG HU

Submitted to the Office of Graduate Studies of
Texas A&M University
in partial fulfillment of the requirements for the degree of

MASTER OF SCIENCE

May 2012

Major Subject: Mechanical Engineering

Synthesis and Characterization of

Magnesium-Silicon and Magnesium-Tin Solid Solutions for Thermoelectric

Applications

SYNTHESIS AND CHARACTERIZATION OF MAGNESIUM-SILICON AND MAGNESIUM-TIN SOLID SOLUTIONS FOR THERMOELECTRIC APPLICATIONS

A Thesis

by

FANG HU

Submitted to the Office of Graduate Studies of
Texas A&M University
in partial fulfillment of the requirements for the degree of

MASTER OF SCIENCE

Approved by:

Chair of Committee,	Choongho Yu
Committee Members,	Raymundo Arroyave
	Miladin Radovic
	Yue Kuo
Head of Department,	Jerald A. Caton

May 2012

Major Subject: Mechanical Engineering

ABSTRACT

Synthesis and Characterization of Magnesium-Silicon and Magnesium-Tin Solid Solutions for Thermoelectric Applications. (May 2012)

Fang Hu, B.S., East China University of Science and Technology

Chair of Advisory Committee: Dr. Choongho Yu

The environmentally friendly n-type $Mg_2(Si, Sn)$ thermoelectric solid solutions have a strong potential of commercial utilization in thermoelectric (TE) energy conversion due to their availability, low density (~3.02 g/cm^3), and high stability at middle temperature range (400-600 °C) that are typically observed from waste heat dissipating systems. The bulk materials were prepared from element powders via slow cooking under vacuum condition and current-assisted hot-press sintering. Temperature *vs* time curves have been researched in this thesis for fully reacted magnesium-silicide and magnesium-stannide green ingots with doping materials *i.e.* antimony, bismuth by different doping ratios. These ingots were ground by a high energy ball miller, uniaxial cold pressed into half inch pallets and then sintered by Direct Current-assisted hot pressing. Different synthesis conditions such as ball milling, sintering time, pressure, have been compared by SEM images and XRD tests analysis to figure out optimized process parameters. Several samples' thermal conductivities (κ) were plotted as a function of temperature to study different synthesis strategies and doping materials' effects on phonon scattering inside bulk thermoelectric materials.

DEDICATION

To my parents, my big family and my friends

ACKNOWLEDGEMENTS

I am deeply indebted to my advisor Dr. Yu for his knowledge, assistance and patience through the course of this research. I would like to greatly appreciate Dr. Arroyave, Dr. Kuo and Dr. Radovic for consideration as my committee members. And I also want to thank my partner Abdullah, my group-mates: Xiong, Advaith, Kyoungwho and Liang for their help.

Finally, thanks to my mother, father and big family for their encouragement and support, to my dear friends for their kindness and love.

NOMENCLATURE

S	Seebeck coefficient by v/K
V	Voltage by v
ΔT	Temperature difference by K
κ	Thermal conductivity by $W \cdot K^{-1} \cdot m^{-1}$
κ_p	Phonon's part of thermal conductivity by $W \cdot K^{-1} \cdot m^{-1}$
κ_e	Electron's part of thermal conductivity by $W \cdot K^{-1} \cdot m^{-1}$
σ	Electrical conductivity by $S \cdot m^{-1}$
L_0	Lorenz constant (2.44e-8) by $W \cdot \Omega / K^2$
ZT	Figure of Merit value of thermoelectrics
v_{sound}	Speed of sound by m/s
C	Specific heat by $J \cdot kg^{-1} \cdot K^{-1}$
l	Mean Free path(MFP) by nm
Q	Heat energy flow by J
A	Area by m^2
L	Heat flow path way by mm
α	Thermal diffusivity
ρ	Density by g/cm^3
C_p	Specific heat under constant pressure by $J \cdot kg^{-1} \cdot K^{-1}$
d	Sample's thickness in Flash method by mm
$t_{1/2}$	Time necessary by μs for the signal to reach 50% in Flash method

$\boldsymbol{\lambda}$	Wavelength of phonon by nm
$\boldsymbol{\lambda_{incent}}$	Wavelength of incent X-ray by nm
$\boldsymbol{\theta}$	Bragg angle by degree
$\boldsymbol{t}$	Interplanar distance of crystalline material by nm

TABLE OF CONTENTS

Page

Page

LIST OF FIGURES

Page

Page

Page

LIST OF TABLES

Page

1. INTRODUCTION AND LITERATURE REVIEW

Finding a sustainable supply of energy to face fossil fuel supplies decrease and world demand increase is becoming a major challenge for world's population. Thermoelectric materials, which involve the conversion between thermal and electrical energy, have developed rapidly in recent decades since 1990s[1]. A significant fraction of energy is lost during power generation and transportation which is the form of waste heat. Total thermal energy rejected to atmosphere is more than 60% of the input energy over world [2]. Waste heat has following common characteristics[3]: dispersed small-scale energy sources with unstable variation, handling difficulty and lower energy density. Since thermoelectric devices only require a temperature difference to produce electric power and have no moving parts required, these materials can easily use low-grade sources of energy.

Thermoelectric devices don't have moving parts and can be adapted with other technology; Whereas most of the electricity-thermo energy conversion efficiencies are low, commercial materials are mostly toxic and cannot work over low temperature range[2] (10s to 400 K) , advanced thermoelectric materials attract so many researchers. Recent reports show that bulk samples containing nanoscale constituents could get improved thermoelectric figure of merit values[1]. This thesis focuses on thermoelectric bulk materials synthesis, and aims to improve their thermoelectric properties by nano-scale constituents introduce.

This thesis follows the style of Applied Physics Letters.

1.1 Thermoelectric Effect and Its Development on Waste Energy Retrieval

Thermoelectric effect was first discovered by Thomas Johann Seebeck in 1821, that electric potential could be generated by a closed loop of dissimilar metals with temperature gradient. The charged carriers either holes or electrons in metals, semiconductors and semimetals are free to move like gas molecules, while carrying heat as well. When a temperature difference is applied on different location of materials, the free charged carriers will diffuse from hot end to cold end. According to different charge there are n-type thermoelectric materials with free electrons and p-type thermoelectric materials with free holes(Figure 1). A measure of the electric potential generated from unit temperature difference is defined as Seebeck coefficient S, which is one of essential thermoelectric criteria:

$$\mathbf{S} = \frac{\boldsymbol{V}}{\Delta \boldsymbol{T}} \tag{1}$$

Where $\boldsymbol{V}$ is the produced voltage, and $\Delta \boldsymbol{T}$ is temperature difference.

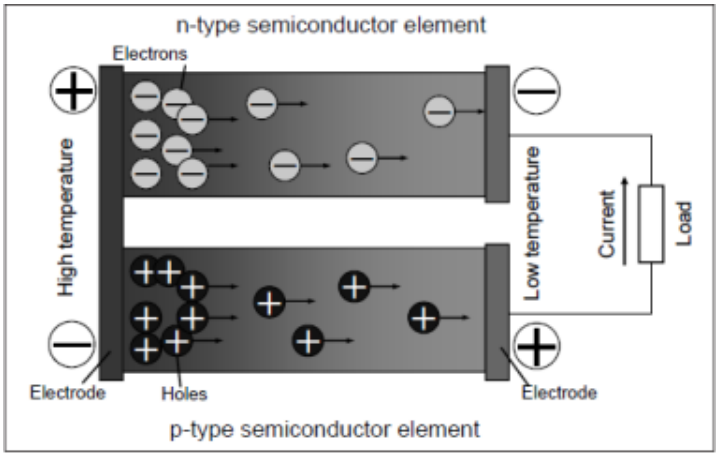

Figure 1 Mechanism of n-p junction

Figure 2 shows a very typical thermoelectric device composed by many thermoelectric couples. These couples are wired in series to make close electrical cycle and different temperatures on each side of parallel. Temperature difference generates heat flow which provides electrical current from Seebeck effect.

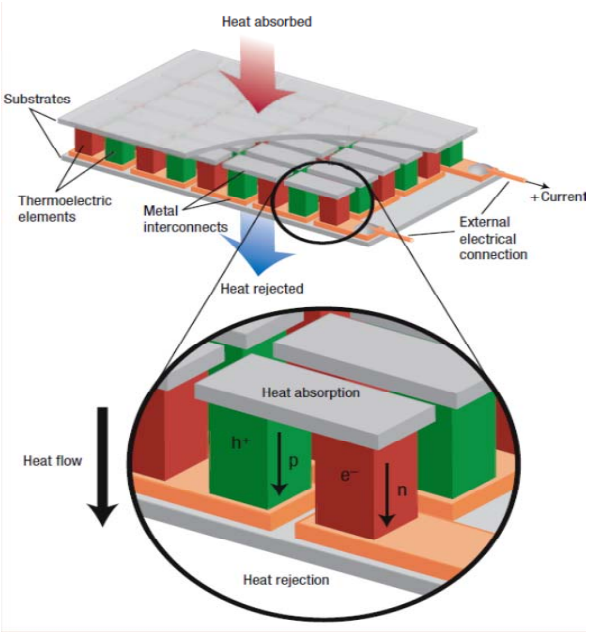

Figure 2 Thermoelectric module of energy & cooling generation [4]

Meanwhile a higher electrical conductivity to reduce the joule heating energy loss and a lower thermal conductivity to keep large temperature gradient across the n-p junctions are also needed for good thermoelectrics. Since both electrical conductivity $\boldsymbol{\sigma}$ and electron's part of thermal conductivity $\boldsymbol{\kappa_e}$ keep the same trend of change according to Wiedemann-franz law[5]:

$$\frac{\boldsymbol{\kappa_e}}{\boldsymbol{\sigma}} = \boldsymbol{L_0} \times \boldsymbol{T} \tag{2}$$

$\mathbf{L_0}$ is the proportionality constant called the Lorenz constant (2.44e-8) and has the units $W \cdot \Omega / K^2$. Lower concentration of carriers exhibits higher Seebeck coefficient but lower electrical and thermal conductivity. To optimize above three factors, a merit of figure has been suggested as:

$$\boldsymbol{ZT} = \frac{\boldsymbol{\sigma \times S^2 \times T}}{\boldsymbol{\kappa}} \tag{3}$$

To get a higher ZT value, we need higher Seebeck coefficient and higher electrical conductivity as well as lower thermal conductivity. However, according to Wiedemann-franz law, such paradox is hard to be solved. Low dimensional materials have shown the promise of solution to the paradox of bulk materials since middle 20th century raise by Wiedemann-franz law of thermal conductivity and electrical conductivity and will be future discussed in section 1.2.

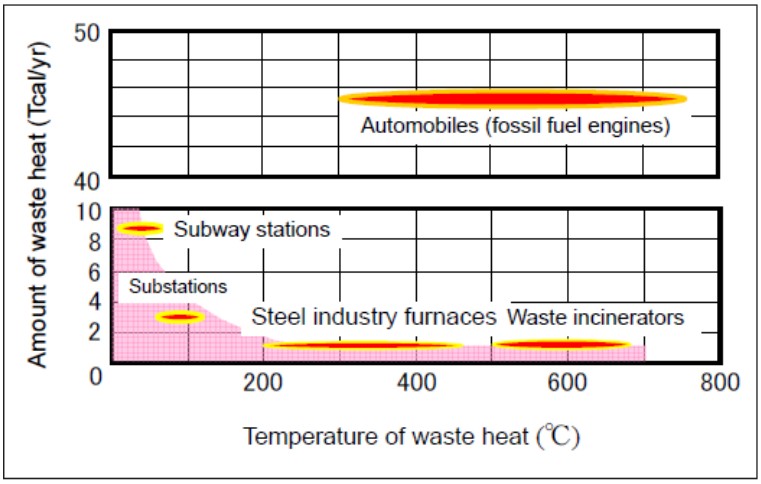

Figure 3 Temperature range and annual amount of waste heat generated in Japan[6]

Fossil fuel is the mainly energy source of world, whose utilization has virtually reached its limits and demand keeps increasing. Therefore, use of waste heat energy is

the only means of achieving further energy use efficiency and the main way to reduce greenhouse gases, even the total efficiency of thermoelectric conversion system is low. Figure 3 shows the relationship between temperature of the waste heat and the annual amount of waste heat in various types of Japanese social systems. This data is reasonable for comparison with American society. Large-scale waste energy recovery of >200 C temperature range has well developed in recent years but there is still a large zoom to increase conversion level. Nano-composites' introduce as high ZT value (>1) of p-type bismuth antimony telluride bulk alloys, shows possibility of thermoelectrics' application[7,8].

Worldwide, more than 90% of large-scale power generating systems employ fossil fuels as main heat source, generating efficiency is 40-60%[6], *i.e.* combined cycle using gas turbine and steam turbine. Almost half heat of combustion of fossil fuels is waste heat. Figure 4 shows the typical energy path for vehicles with gasoline-fueled internal combustion engines and only a quarter of energy is used to drive car. The 40% exhaust heat flow and 30% coolant flow could be retrieved by thermoelectric generator to provide electrical power of revalorize automotive heating, ventilation and air-conditioning. In generally speaking the average exhaust gas temperature for various vehicles is between 500 and 600 ˚C, in which is supposed to be most effective of magnesium silicide's thermoelectric materials[9].

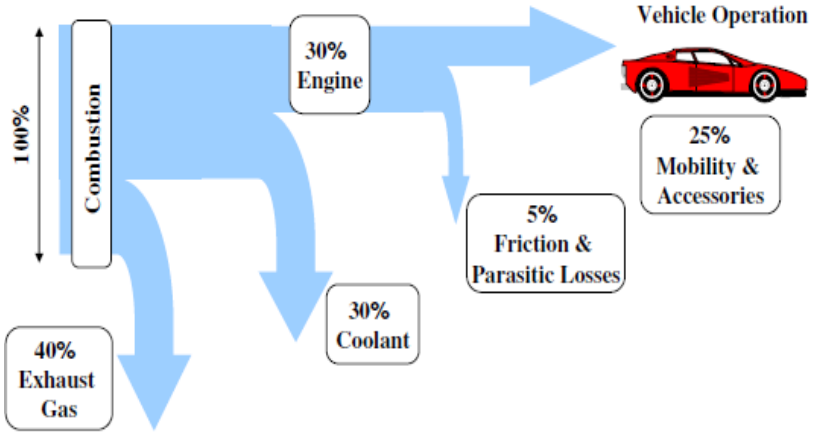

Figure 4 Typical energy path for vehicles with gasoline-fueled internal combustion engines[10]

1.2 Phonon Scattering and Thermal Conductivity

The way to improve ZT value is via low dimensional structuring either nano-scale materials or nano-scale structures. To better understand the strategy of increasing electric conductivity without dramatic increasing thermal conductivity, a conception of phonon should be introduced. There are two parts of thermal conductivity: one is electron part which is tightly related to electrical conductivity according to equation (2); the other is phonon part which has less effect on electrical conductivity. And in thermoelectric materials, phonon's thermal conductivity is dominant over RT to medium temperature[5].

1.2.1 Phonon scattering

A phonon is a quantum mechanical description of a special type of vibrational motion, in which a lattice uniformly oscillates at the same frequency, and atoms vibrate naturally around their equilibrium lattice points[11]. According to "Uncertainty Principle"

in quantum mechanics, atom's positions are unknown; meanwhile unsure plane wave amplitudes are statistical distribution at a given temperature.

In classical mechanics this is known as normal mode, by which lattice vibration can always be analyzed in terms of plane waves focusing on phonons' motion and transmitting. Considering a solid to be a periodic array of mass points, due to the connections between atoms, the displacement of atoms from their equilibrium positions will give rise to a set of vibration waves propagating through the lattice, shown in figure 5, and **λ** is wavelength of phonon. With the phonon interpretation, the lattice vibration wave has been quantized in terms of particle-like phonons as well.

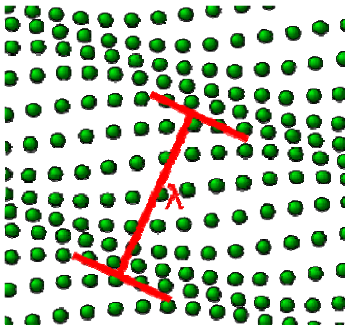

Figure 5 Phonon propagating through a square lattice by exaggeration [12]

The thermal conductivity can be calculated from following equation:

– (4)

Where is the speed of sound; ***C*** is the specific heat which shows the capacity of holding thermal energy in unit mass per unit temperature difference; ***l*** is the mean free path for phonons and electrons, which is the average length of energy package/electron can go ahead without collision with other or defects. Therefore phonon scattering

mechanisms strongly affect solid thermal conductivity. There are three types of phonon scattering: phonon-phonon scattering, phonon-electron scattering and phonon-imperfection scattering, where imperfections include grain boundaries, defects and the material interfaces.

Phonons in materials have different spectrum of wavelengths, *i.e.* the energy of phonon package, and mean free paths, each of which contributes to the total thermal conductivity. The characteristic size of scattered centers for phonons with different energy and mean free path lengths are varied. Impurity atoms which characteristic size is around several angstroms are most effective in scattering phonons because phonons' dominant wavelength is around 1 nm[11]. Then larger characteristic length than impurity atom which is supposed to be tens to hundreds nanometers is introduced for phonons scattering by reducing the mean free path. Characteristic length for certain phonon scattering center should be matched to phonon mean free path to achieve effective scattering[13]. Further examples about nanostructured thermoelectric materials will be discussed in section 1.3.

1.2.2 Thermal conductivity measurement

Thermal conductivity $\boldsymbol{\kappa}$ is an intrinsic property of a material presenting its ability to conduct heat, which is defined as the quantity of heat (**Q**) transmitted through a unit thickness (***L***) in a direction normal to a surface of unit area (***A***) due to a unit temperature gradient ($\boldsymbol{\Delta T}$) under steady state conditions and when the heat transfer is dependent only on the temperature gradient.

$$\boldsymbol{\kappa} = \frac{\mathbf{Q}\times\mathbf{L}}{\mathbf{A}\times\Delta\mathbf{T}} \tag{5}$$

Absolute axial heat flow method or called “divided bar method” is most widely used for measurement at low temperatures and modern equipment changes little in principle from that used by Lees more than 80 years ago[14] shown in figure 6. In this method all the heat supplied to the source Q is conducted along the rod of uniform cross section A and distance L between thermometers to upper heat sink, temperature gradient has been established as $\Delta T = T_2 - T_1$, then sample’s thermal conductivity should refer to equation(5):

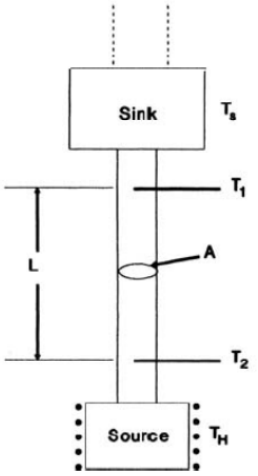

Figure 6 Schematic of axial heat flow apparatus[14]

This measurement assumes that the temperature is uniform across any element of the cross section, and the heat losses by conduction through any residual gas, by electrical leads from T_1 and T_2 (thermoelectric effect), and by radiation are negligible. The choice of specimen geometry is dictated by the conductivity to be measured, by thermometer sensitivity and by the maximum and minimum values of **Q** that can be tolerated. Practically the length ***L*** should be large enough comparing to sample’s

diameter. To reduce equilibrium time for low conductivity materials like thermoelectric materials, L/A is made small such as 10^{14}.

Thermal conductivity tests by steady state method are not only hard to achieve, but time consuming due to steady-state conditions are invariably required no matter what technique applies, meanwhile the precision cannot be guaranteed because assumption mentioned above is hard to approach especially for low thermal conductivity materials. Therefore a non-steady-state measurement method using thermal diffusivity techniques has developed recent decades. Then the determination of basic thermal transport data can be realized from

$$\boldsymbol{\kappa = \alpha \cdot \rho \cdot C_p} \tag{6}$$

Where $\boldsymbol{\alpha}$ is the thermal diffusivity, $\boldsymbol{\rho}$ is density and $\boldsymbol{C_p}$ is specific heat. The advantages are extreme rapidity and the ability to generate large volumes of data very quickly. Meanwhile heat losses which are tightly related to test time have a smaller influence when actual measurement times a short and are generally amenable[14]. Thus diffusivity techniques are now widely used for measurement above RT on bulk materials especially on thermoelectric materials. To get more accurate results, heat capacity of samples should be achieved by Differential Scanning Calorimetry(DSC)[15]. There are several representative techniques used non-steady-state methods, Angstrom's method, thermal conductivity probe, transient hot wire[16] and Laser Flash method.

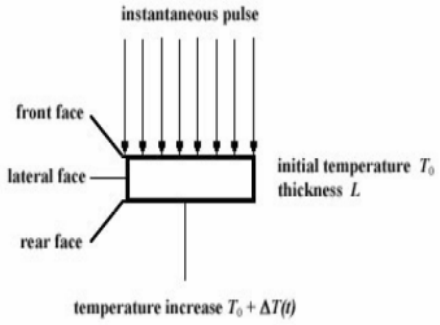

Figure 7 Schematic of Laser Flash Method

As shown in figure 7, one face of sample is irradiated by a short pulse of heat from a laser, irradiation times being less than 1 msec. Then Flash method eliminate the problem of the thermal contact resistance, while the heat losses are minimized by marking in a short enough time so that heat loss can be ignored. The resultant temperature raise of the opposite surface is recorded, from which the thermal diffusivity is computed from the characteristic time dependence of temperature rise by Parker's formula[17]:

$$\boldsymbol{\alpha} = \frac{\mathbf{1.38}\times \boldsymbol{d}^{\mathbf{2}}}{\boldsymbol{t}_{\mathbf{1/2}}} \tag{7}$$

Where $\boldsymbol{d}$ is the sample's thickness and $\boldsymbol{t}_{\mathbf{1/2}}$is the time necessary for the signal to reach 50% of its maximum value. Physically speaking the thermal diffusivity is heat propagating speed through a material.

In Laser Flash Analysis(LFA), the sample size can be as small as 12 by 5 mm. Sample's thermal diffusivity has a very broad range from 10e-3 to 10 cm^2/s. It can be used to test samples up to much higher temperature range than steady-state methods even through the melt in some cases. However, expensive device cost due to heat pulse

generation, optical detection and the high speed data acquisition limits Flash Laser method's widely using. Another worse limitation is porous and non-homogeneous materials cannot achieve so accurate data through general Flash method[18].

1.3 Improvement by Nanostructured Materials

Traditional method to improve ZT is to discover new thermoelectric materials. Some of classical materials such as Bi_2Te_3, SiGe, PbTe *etc* have be commercially used. To fix their drawbacks, such as expensive of raw materials, toxic bringing handle dangerous, effective on relatively high temperature range, a new thermoelectric material system has been researched in this literature; further discussion is shown in section 2.2.1.

Physical explanation of different phonon scattering center' characteristic length mentioned in section 1.2 draws a promise picture of why nanocomposite is able to beat the alloy limit and further reduce thermal conductivity. The conception of low-dimensional thermoelectric materials was introduced in early 1990s. Well modification to the thermal properties of low dimensional material can be used to improve ZT value of the material. Hicks *et.al*[19] suggested a directional nanowires thermal transport model, which is straightly explain the pathways to electrons confined to move along length direction and restricts of phonons flows by scattering on the wall of nanowire. Thus electrical conductivity can be maintained or less decreased while the lattice thermal conductivity can be dramatic reduced then ZT value increase.

The nano-sized interfaces affect phonon transport which attracts more and more interests. Due to "Quantum confinement effect", the thermal conductivity low limit called "alloy limit" derived from classical theory is also turned out to be wrong in nano-

structured composites[20]. On one hand, Nano-structured thermoelectric materials have been shown their abilities to reach a lower thermal conductivity than that of bulk counterparts, such as silicon nanowire[21] (1D nanostructure), silicon thin film[22] (2D nanostructure) *etc*. A figure of merit ZT=2.4 has been reported in Bi_2Te_3/Sb_2Te_3 quantum well supperlattices[23], which is supposed to be one of the highest ZT values of thermoelectric system.

On the other hand, the needs of macroscopic dimensional thermoelectric materials increase because of lower manufacturing cost and more convenience to assembling. Therefore, achievements of bulk solid solution systems contained nano-scale compositional modulations have generated many reports. The enhancement of ZT value is mainly due to the reduction in the lattice thermal conductivity by increased scattering of intermediate wavelength phonons at nanosized grains and by the point defects scattering of short wavelength phonons.

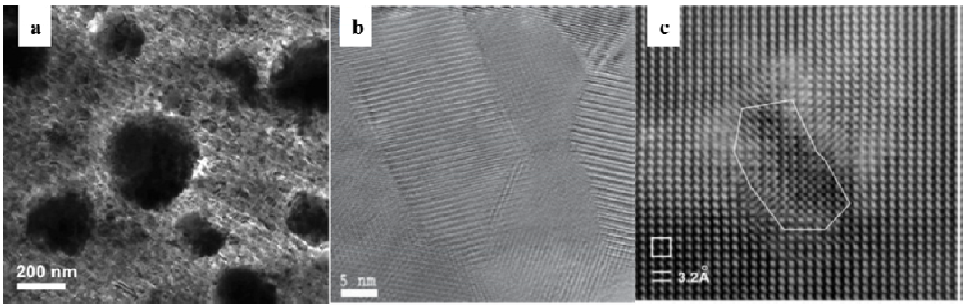

Figure 8 Nanostructured in bulk thermoelectric materials
a. TEM image of the typical DC hot-pressed nanostructured dense bulk samples[24]
b. TEM image of random orientationed and clear grain boundaries in bulk BiSbTe[7]
c. TEM image of $AgPb_{18}SbTe_{20}$ sample showing a Nano-sized region of the crystal structure[25]

In higher temperature range (>700 °C), a p-type nano-structured bulk alloy $Si_{20}Ge_{80}$ achieves a significant ZT enhancement of about 1 at 800~900 °C[24]. Nanodots of hundreds nanometers have been embedded in bulk matrix shown in figure 8(a). In lower temperature range (RT to 250 °C), ZT value of p-type BiSbTe thermoelectrics which starts from 1.2 at RT, peaks at 1.4 at 100 °C and decreases to 0.8 at 250 °C has been achieved in Poudel *et.al*'s work[7,8]. High magnification image figure 8(b), shows the nano-grains with high crystallity, random orientation and clear grain boundaries are about tens nanometers, increasing interfaces increases phonon scattering then reduce thermal conductivity. In bulk thermoelectric materials, the highest ZT value is reported to be 2.2 at 527 °C of powder annealing ingots in n-type $AgPb_mSbTe_{2+m}$ system[25]. As shown in figure 8(c), the nano-sized region is around tens of angstrom which is comparable to phonon's wavelength and can bring huge phonon scattering. They got nano-powder from ball milling as mechanical alloying, then prepared bulk disks by Spark Plasma Sintering(SPS) or direct-current(DC) introduced hot pressing. Such synthesis methods have been chosen in this literature and detailed discussion will be shown in section 2.

1.4 Powder Metallurgy Development

Powder metallurgy is defined as the process in which powders are mixed by wanted ratio, compacted and then sintered at elevated temperatures in controlled atmosphere to form a dense body[26]. The powder metallurgy process generally consists of four basic steps: powder manufacture, blending, compacting and sintering. The controllable characteristics of powder metallurgy products include mechanical, thermal,

electrical and other unconventional properties of materials as aggregates semiconductor and intermetallic compounds, thus powder metallurgy is a promising technique to get enhanced thermoelectric bulk materials with well-steerable grain or micro- even nano-structure[2]. Comparing to thermoelectric film deposition technique, it has following advantages:

i. Begin with materials powder, clay or chunks with very high levels of purity and uniformity which can be prepared by comminution, grinding, chemical reactions or electrolytic deposition[26] as well as absence of binding material needed, relatively straightforward to achieve high density, designed composition and preservation of purity.

ii. Higher identification and easier control of key process parameters (temperature, pressure, protect atmosphere and time) which are required to achieve stable reproducibility.

iii. Relatively higher fabrication rate, high product uniqueness---- this is much better than thin film technology---- and less expensive equipment investment. Product cost effectiveness of powder metallurgy wins the competition because of its lower energy consumption, higher material utilization and reduced dimensional tolerance control in the sintered product[27].

iv. Easier manufacture input, powder metallurgy equipment such as pressing machines, funaces, vacuum or atmospheres *etc*[28], are feasible in either industrial manufacturer or lab experiment; the bulk products shown better

mechanical properties over certain temperature ranges leading to easier system integration and longer device lifetime.

1.4.1 Liquid phase sintering and solid-state sintering

The driving force of sintering is reduction of surface free energy in composite system, but actual occurrence of sintering requires transport of matter. In crystalline solids, matter transport occurs by diffusion of atoms, ions, or molecules along definite paths. Sintering of crystalline materials can occur by at least six mechanisms as: vapor transport, surface diffusion, lattice diffusion, grain boundary diffusion and plastic flow, among which grain boundary diffusion and lattice diffusion are important densification mechanism in metals and ceramics. These diffusions from the grain boundary to the neck, along with plastic flow cause neck growth then densification.

Grain boundaries in polycrystalline materials are important factor to effect solid-state sintering; because mass transport by vacation diffusion is to reduce the curvature of grain then to reduce internal system free energy, so presence of grain boundaries can influence the mass transport during sintering. Grain boundaries act as vacancy sinks by virtue of their intrinsic disorder to facilitate pore shrinkage and densification.

Liquid phase sintering is an important ceramic consolidation technique and widely used to fabricate various ceramic components. In liquid-state sintering, at least one but not all elements are in a liquid state, which is quite useful to process solid solution with high-melt point constituent. It's necessary that the major phase should be at least slightly soluble in the liquid phases; otherwise the grains rearrangement would not happen. There are three main stages of liquid phase sintering[29]:

i. Melting phase spreading and penetration into solid phase; rearrangement of grains into a more favorable packing order by the melting liquid capillary action,;

ii. Solution-Precipitation of unmelt powder in areas of low chemical potential where particles have lower concentration, which is very similar to “Contact flattering” of grain boundary diffusion in solid state sintering. Smaller particles will go into solution preferentially and precipitate on larger particles which is called “Ostwald ripening” occurred in solid or liquid solution systems[30]. This process describes initial powder mixture from inhomogeneous structure to homogeneous over time.

iii. Final Densification of solid skeletal network, pores removal by simultaneous liquid movement from efficiently packed regions into macropores. While the mixture of solid particles and liquid sinters together, the porosity of the powder compact gradually diminishes to form a dense component.

The primary advantage of liquid phase sintering is the enhanced kinetics of sintering, which can be carried under lower temperature to sinter solid powders which are hard to be sintered by solid-state sintering. Meanwhile, it’s an important method to get tailored microstructures ceramic alloys.

1.4.2 High energy ball mill

Ball milling is an effective top-down approach to obtain fine particles widely used in industry and lab research. Comparing to conventional ball milling resulting particles size from one to several micrometers, high-energy ball milling developed since 1970s can create nanoparticles from ingots in relatively short time with a size as small as several nanometers[31,32].

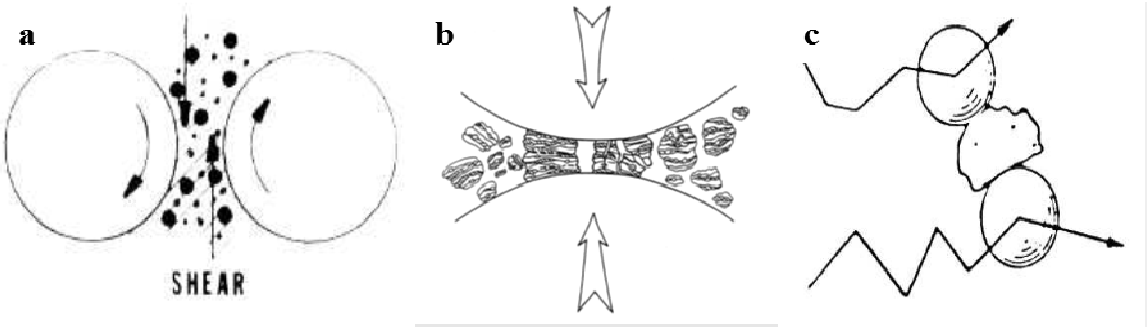

Figure 9 Ball-Powder-Ball collision mechanisms during ball milling
a. Shear force; b. Impact force[33]; c. Irregular movement by shaking high energy ball milling[34].

During ball milling the powder particles are repeatedly flattened, cold welded, fractured and re-welded. Whenever two balls collide, some amount of powder is trapped in between them. Shear force is present due to balls random movement of different rotation (figure 9(a)). The force of the impact also plastically deforms the powder particles leading to fracture shown in figure 9(b). The new surfaces created enable particles to weld together again leading particle size increasing. In early milling stages, the particles are normally soft, they have more tendency to weld together to form large aggregation. With continued deformation, the particles get work hardened and fracture by a fatigue failure or by the fragmentation of fragile flakes. Particles sizes mainly

reduce at this stage. After certain period as shown in figure 10, a few minutes to hours, the rate of refinement of the particle internal structure reduces due to cold welding predominates over fragments; strong agglomerating forces dominate if possible and particle size may even increase after too long time milling.

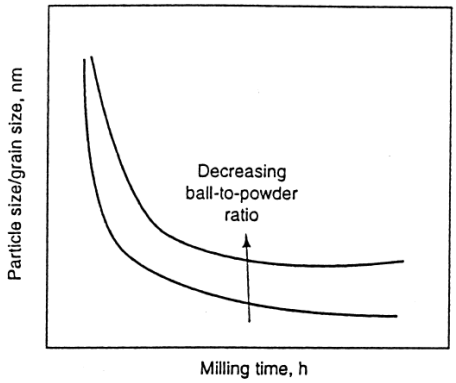

Figure 10 Refinement of particle and grain size with milling time[33]

In general, plastic deformation during ball milling proceeds by slip and twinning at low and moderate strain rates, whereas at high strain rates, the deformation of shear bands, which consist of dense network of dislocations, becomes the dominant deformation mechanism[32]. Figure 9(c) shows the irregular movement by shaking high energy ball milling which can provide higher impact velocities and frequencies of balls and much more shearing action. High energy ball milling could accelerate the process from high dense of dislocation resulting sub-grains disintegration to deformation occurring in shear bands; these bands exist in previously unstrained parts of materials. From two or three steps mentioned above, nanocrystalline particle can be achieved, but future refinement seems to be impossible[32].

Meanwhile, the efficiency of particle size reduction is very low, even in high-energy ball milling processes it could not achieve 1%. The remaining energy is lost mostly as heat[33]. That's why there are always temperature rising phenomena along with ball milling, and specially cooling systems are required for high energy milling systems especially.

1.4.3 Uniaxial cold compaction

Consolidation of metal or ceramic powders into useful products generally need powder compaction step, which converts powder from a loose aggregate into a dense compact that has sufficient green strength to the following process operation. Uniaxial cold compaction in a rigid die is the most prevalent method for powder metallurgy parts production because such compaction is cost effective with relatively straightforward tooling[35]. In uniaxial compaction, pressure is applied to the powder only with punches that move in the vertical direction within rigid die. Cold pressing in rigid dies has advantages of dimensional control due to the well-defined hole size, high compaction pressures due to hydraulic pressing equipment, process repeatability due to mechanization[35].

The controlling parameters of cold compaction samples qualities are mainly geometric distortion of the pressed component, container dimension and the material's ability for plastic deformation[35]. Compaction technique often causes powder deformation as following steps: rearrangement, distortion (plastic deformation) and fracture. Figure 11 shows uniaxial compaction in hole shape die.

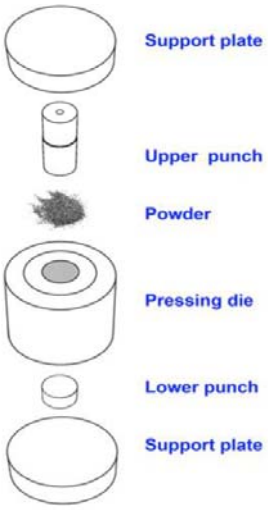

Figure 11 Uniaxial cold press with rigid hole die [36]

Ceramic powders are more difficult to compact than metals due to high level of residual stresses in ceramic powders leading to fracture upon subsequent handling even applied very high pressure during cold press[37]. Meanwhile, nanomaterial is hard to achieve wanted green density by cold press due to its difficulty for strain hardening by restricted dislocation generation and flow[38]. Nanoparticles are also shown capable of withstanding a high hydrostatic pressure without suffering heavy damage[39]. The smaller the powder size, the stronger inter-particle friction and bridging effect which hinder densification. Thus much more work should be done to achieve full density bulk sample from nano-sized ceramic powder.

1.4.4 DC-assisted hot press

Sintering is composed of both densification and grain growth. As mentioned above, to increase the densification rate and reduce the porosity, external pressure and increasing temperature are necessary.

Currently, the use of the electric current to aid pressure assisted sintering of materials is under lots of investigation. The main electric current assisted sintering processing is known as spark plasma sintering, although plasma happening is uncertain[40]. Comparing to traditional sintering, current assisted hot pressing has following advantages: faster heating rate, lower sintering temperature, shorter holding time, consolidation of difficult-to-sinter-powders, reduce the needs of sintering binders, less sensitivity to initial powders characteristics, and markable improvement of consolidated samples[40]. Meanwhile, due to shorter process period, air sintering often result appropriate results with no atmosphere protection[40], which could greatly cut down the device cost.

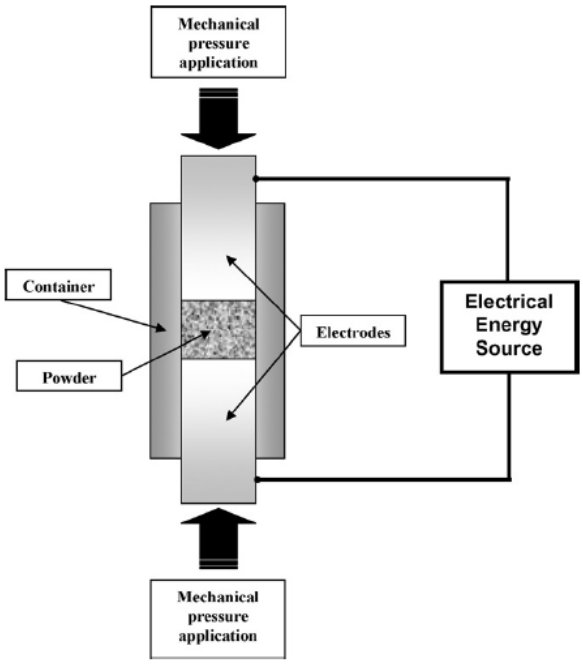

Figure 12 Schematic representation of the Electric Current Assisted Sintering process[40]

Comparing to hot pressing which sample container is typically heated by radiation from the enclosing furnace through external heating elements and convection of inert gases if applicable. Therefore, the heating rate is typically slow due to lots of heat is wasted. Because the heat transfers from outer part to internal part of sample needs sometime, limitation of sample size and inhomogeneous grain size growth are another drawback for hot pressing. Electric current assisted sintering (figure 12) is characterized by the efficient use of the heat input. The enhancement of mass transport by electromigration makes possible the sintering of extremely refractory materials. Lower temperature and hold time make it possible to sinter nanosize powders to near theoretical values with little grain growth[41].

2. SYNTHESIS OF MAGNESUM-SILICON-TIN BASED SOLID SOLUTION

2.1 Magnesium Silicide Materials and Doping Material Choice

The field of thermoelectrics developed rapidly since 1950s when the basic science become well established[1], the important role of heavily doped semiconductors as good thermoelectric materials became commercialization, such as Bi_2Te_3 and $AgPb_mSbTe_{2+m}$. However, these materials are relatively heavier, expensive and toxic comparing to Mg_2X, where X=Si, Ge or Sn.

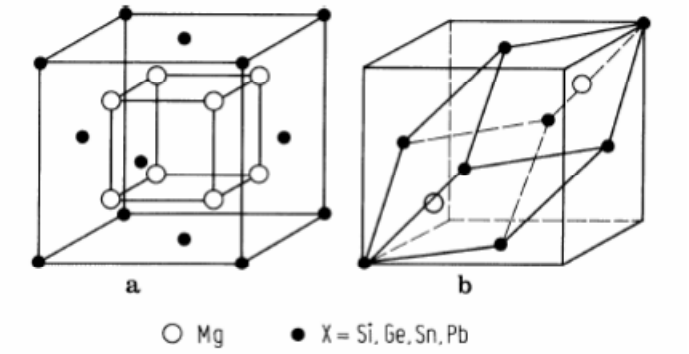

Figure 13 The Antifluorite lattice of the Mg_2X-compounds:
(a) FCC sublattice of the X-atoms (lattice constant *a*) & simple cubic sublattice of the Mg-atoms (lattice constant *a*/2); b) primitive cell.[42]

The thermoelectric properties of Mg_2X semiconductors, have been studied widely. All crystalline are the calcium fluoride structure Fm3m as shown in figure 13. The electropositive magnesium atoms occupy the sites fluoride, while the electronegative group IV metals occupy the calcium atom sites. The lattice has face-

centered-crystalline (FCC) translational symmetry. They have similar lattice parameter so that substitution of this system is most like to be solid solution mechanism.

As a potential important thermoelectric system, intermetallic silicide compounds attract increasing research recent years due to the cost and abundance of its constituent elements, environmental friendliness, and high-temperature oxidation resistance[43]. Also due to Mg_2X's low density, reasonable achievability, cheap starting materials, capacity to operate in air and in vacuum and most important, environmentally friendly, magnesium-silicide and magnesium-stannide solid solution system is promising candidates to replace Pb-Te[44] and TAGS (scrambled acronym for GeTe/AgSbTe2 alloys)[25] in the middle range of operation temperature. Figure 14 shows ZT curves over temperature of typical n-type thermoelectric materials.

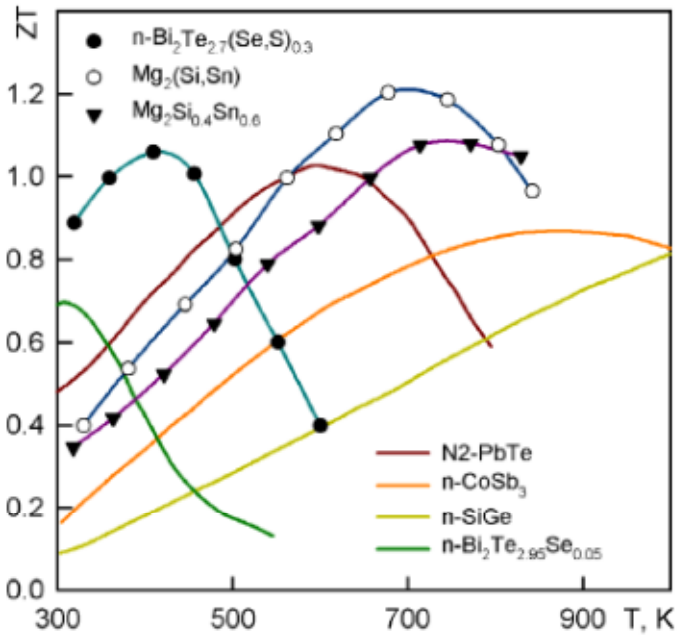

Figure 14 Temperature dependence of dimensional figure of merit of typical n-type thermoelectrics [9]

In Zaitsev[9,45,46] papers, Mg_2X were supposed to be the perspective materials for thermoelectric generators at moderate temperature. Conduction band structure and transport properties of n-type Mg_2Si-Mg_2Sn solid solutions have been studies. It's shown that the system is a favorable base for the creation of excellent thermoelectrics with band type of conductivity. Because the Mg_2Si and Mg_2Ge compounds along with high enough melting point then have rather high values of energy gap and mobility, *i.e.* too high thermal conductivity, which does not allow to be pure thermoelectrics compounds.

Table 1 Properties of Mg_2X compounds[47]

	Mg_2Si	Mg_2Ge	Mg_2Sn
Melting point, K	1375	1388	1051
Spacing, A	6.338	6.3849	6.765
Density, g cm^{-3}	1.88	3.08	3.59
ΔE, eV	0.4	0.58	0.16
κ_L, W m^{-1} K^{-1}	7.9	6.6	5.9

Mg_2Si and Mg_2Sn are chosen because of their maximum difference in molecular mass which leads the lowest lattice thermal conductivity[48]. The splitted conduction band and a complex valence band of Mg_2Si-Mg_2Sn solid solution system are similar to that of silicon or germanium. These sub bands are separated by gap ΔE. From table 1 one can see the ΔE is low enough for thermoelectricity, which is typically ~0.16 eV in Bi_2Te_3. Also table 2 shows $Mg_2Si_{0.4}Sn_{0.6}$ has relatively good electron structure. Then Mg_2Sn rich $Mg_2Si_{0.4}Sn_{0.6}$ composition has been chosen as base solid solutions as shown in figure 15 when Mg_2Sn = 0.6 under 800 ºC.

Table 2 Parameters of electron structure for $Mg_2Si_xSn_{1-x}$ solid solutions[45]

x	Eg (@ 0K), eV	ΔE, eV	κ_L, W m^{-1} K^{-1}
0.4	0.61	0.07	2.0
0.6	0.68	0.18	2.0
0.7	0.70	0.24	2.0
0.8	0.73	0.29	2.1

Average ZT value of 0.8 is achieved over 350-830K temperature range by high-frequency heated $Mg_2Si_{0.4}Sn_{0.6}$ samples. Here mass fluctuation has been proved to be the primary phonon scattering mechanism in the undoped compounds $Mg_2Si_{0.4}Sn_{0.6}$[9].

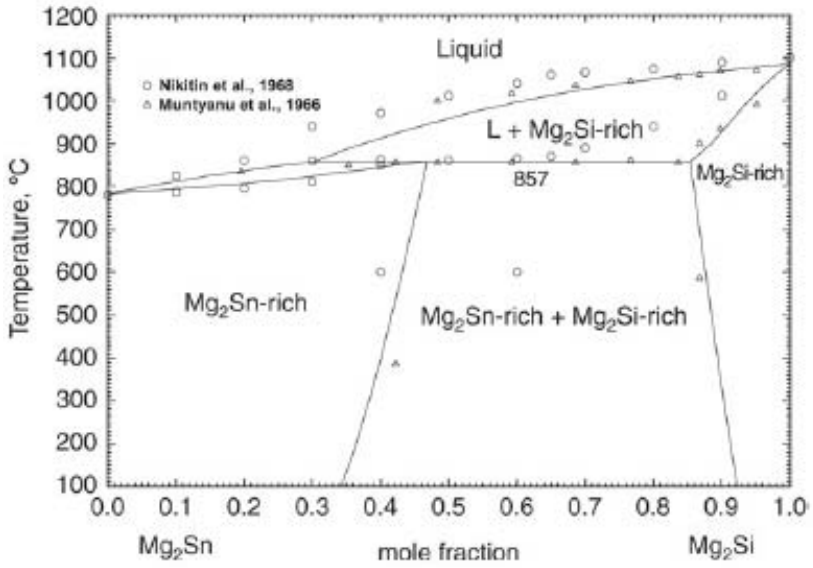

Figure 15 Optimized phase diagram of Mg_2Si-Mg_2Sn solid solution system[49]

Different doping levels have different control factors to enhance ZT value. For example, in PbTe system heavy doping leads large electron scattering on the nano-scale interfaces between metallic islands and matrix thus Seebeck coefficient is dramatically

improved then the ZT value[50]. While in low doping level, ZT value is improved by the reduction of phonon thermal conductivity on interfaces. It's similar that in magnesium-silicon-tin solid solution system ($Mg_2Si_xSn_{1-x}$), different x values with different doping materials have been researched as shown in figure 16.

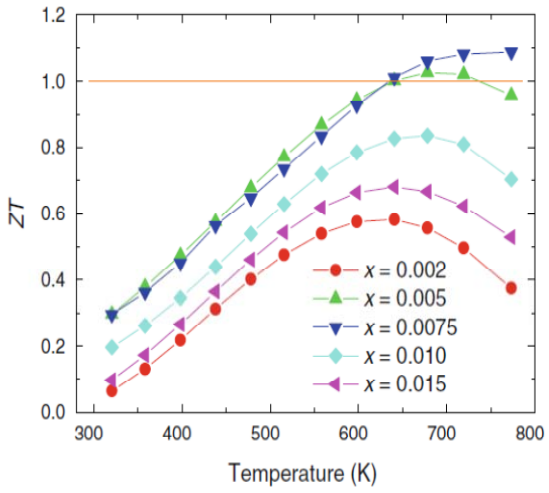

Figure 16 Temperature dependence of figure of merit ZT for $Mg_2Si_{0.4-x}Sn_{0.6}Sb_x$ [51]

Comparing to Zaitsev's samples which were processed by traditional direct melting powder metallurgy, Zhu[51] and Zhang[52,53] have shown improvement of same solid solution system by advanced sintering processing including powdering and SPS. ZT value of their advanced nanostructured magnesium-silicon and magnesium-tin solid solution bulk samples can reach 0.8-1.2 over 500-800K temperature range with antimony doping by effective modulation the band structures. Meanwhile antimony doping also introduce different natural nano-structures to further improve phonon scattering. Figure 17(a) and (b) results from then nanoscale compositional fluctuation. Figure 17(c) and (d) shows embedded nanodots with characteristic length scale of

~10nm. Both of them can enhance the phonon scattering and then improve the ZT values. Embedded nano-structures' interface potential comparing to host materials, inclusion volume fraction as well as characteristic size are key parameters for a good nanocomposite.

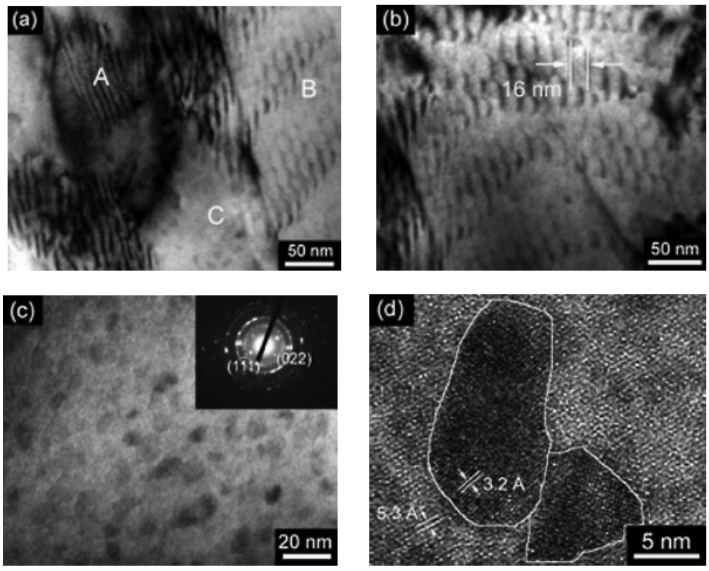

Figure 17 TEM images of hot-pressed $Mg_2Si_{0.3925}Sn_{0.6}Sb_{0.0075}$ with different natural nano-structures: (a) different natural nanostructures; (b) structural modulation with the feature size of ~16 nm in B region of (a); (c) & (d) nanodots of ~10 nm embedded in the matrix[52].

Another doping material bismuth has been chosen due to it is in the same column of antimony in chemical periodical table and has a heavier atomic weight, which is designed to be impurity and to introduce more mass fluctuation for phonon scattering, and its extra electron on the outer atomic orbital will improve the electron mobility as antimony doping.

2.2 Direct Current Assisted Hot press Sintering for Mg-Si-Sn Bulk Plate

It's hypothesized that the use of traditional powder metallurgical techniques to make bulk materials with nanocrystalline structures will improve ZT value of samples[1]. And also due to easier handle and high repeatability of powder metallurgy techniques mentioned in section 1.4, this thesis has chosen it to process magnesium-silicide and magnesium-tin solid solution nano-structured bulk samples.

The thesis mainly aims to reduce thermal conductivity by increasing phonon scattering centers in bulk materials, that's why nano-particles and nano-scale defects were tried to be introduced in samples. The suitable doping materials' effects on thermal conductivity have been researched as well. In early experiment period, Mg-Si-Sn with or without doping material powder mixture has been ball milled by common mill (50 rpm) for one or two days in air, cold pressed then go to DC-assisted hot pressing. There was certain amount of magnesium oxides introduced shown by relatively strong MgO peak in XRD results. Burying samples in graphite powder and using larger hot pressing die could prevent sample's oxidation in some degree; however, the samples' shape could not guarantee and new containment has been introduced by graphite powder. Because tin has too much lower melting temperature than silicon, the leakage of tin at very beginning of DC-assisted hot pressing and non-fully reaction of silicon even with longer sintering time happened often, which dramatically affected sample's quality. Following flowchart (figure 18) shows the optimized synthesis steps of $Mg_2Si_{0.4}Sn_{0.6}$ based solid solution system.

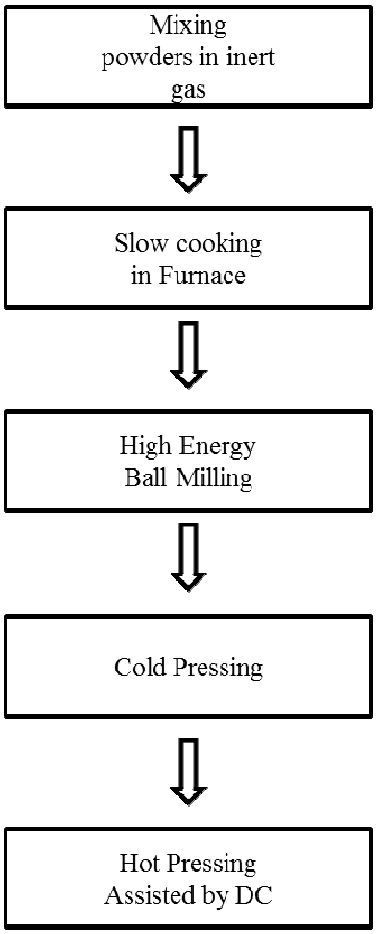

Figure 18 Synthesis steps of magnesium-silicon & magnesium-tin solid solutions

In dry compaction, on one hand a large green density may not always reflect a uniform pore size and distribution. When large agglomerates are present, the green density can be larger than non-agglomerated powders[35]. To break these agglomerates, a critical pressure is necessary. On the other hand, full densification of nanosize powders is likely achieved when all pores are smaller than the critical pore-to-grain size ratio. Large pores usually originate from agglomerated powders and nanoparticles inevitably have a high agglomeration tendency because of their high surface energy[37]. The removal

of large pores requires significantly higher temperature and longer sintering time. So sintering under elevated temperature and high pressure gives distinct advantages in comparison to pressureless sintering to get full density samples.

Grain growth is grain boundary motion and Ostwald ripening increases the average grain size. To increase phonon scattering at interfaces and boundaries to reduce the mean-free-path, grain growth should be controlled. There are two ways to reduce grain growth; one is dopant as impurity which tends to stick to the grain boundaries; the other is fine second phase particles as second phase which are insoluble in the matrix phase.

As thermoelectric materials are conductive, the powders are heated by Joule effect and by heat transfer from the container and electrodes. Joule heating provides high heating rates which can provide a benefit by by-passing the grain coarsening low temperature mechanism[54]. Also the electromigration induced atomic diffusion on particle surfaces can render bulk material with higher density at relatively lower temperature. There are several advantages of electrical current introduced in sintering which includes: including electron wind modification of the diffusion flux, increasing in point defect concentration and reduction in the mobility activation energy for defects[55].

To summary that combination of cold uniaxial press and hot press assisted with electric current is popular method to get nanostructured bulk thermoelectric materials. Meanwhile, small particle size, a more than 80% green density resulted from cold pressing[56] and high pressure during sintering are greatly helpful.

2.2.1 Mg_2Si and Mg_2Sn powder preparation

An ingot of magnesium-silicon or magnesium-tin solid solution with doping materials can be made from high-purity elements powder. Table 3 shows the detail information of each element powder (by *Alfa Aesar Company*). According to liquid phase sintering and solid state sintering introduced above, slow cooking method is chosen in this thesis to prepare $Mg_2Si_{1-n}X_n$ and $Mg_2Sn_{1-m}X_m$ powder.

Table 3 Detailed information of raw element powders

Element	Melting Point / ºC	Particle size / μm	Atomic weight / g mol^{-1}	Purity
Mg	650	44	24.3	99.8%
Si	1414	149	28.1	99.5%(metal basis)
Sn	232	44	118.7	99.8%(metal basis)
Sb	630	74	121.8	99.5%
Bi	272	44	209.0	99.8%(metal basis)

There are three general requirements for liquid phase sintering[57]: i. A liquid must be present at the sintering temperature; ii. There should be good wetting of the solid by the liquid; iii. The solid must be reasonable soluble in the liquid. Although liquid phase sintering process is not an equilibrium process, phase diagram does be an important mean to predict systems with favorable characteristic for liquid phase sintering[58]. Shown in figure 19 Mg-Sn phase diagram, magnesium stannide has a deep eutectic reaction with liquid tin; and there is a large melting difference between tin and magnesium, which is essential for enhanced diffusive transport of the base.

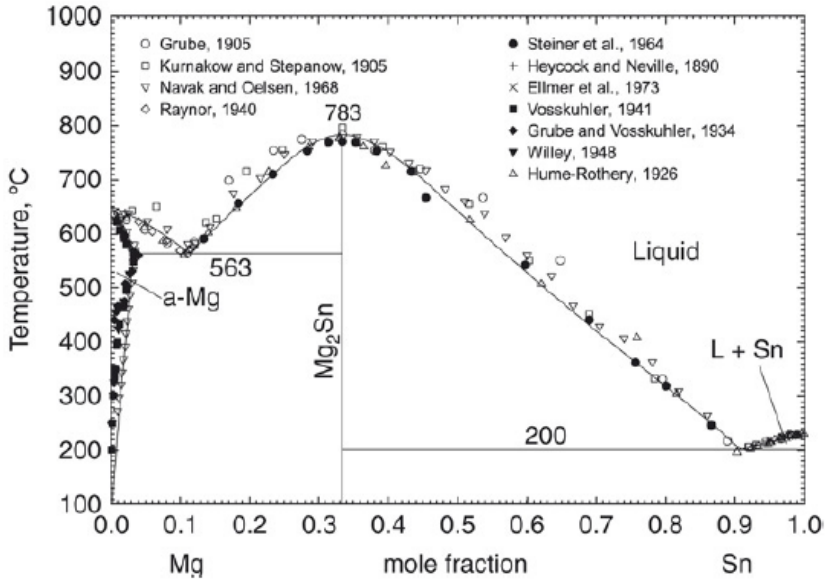

Figure 19 Optimized phase diagram of Mg-Sn binary system[49]

For solid state sintering to initiate, the ions that comprise the ceramic must have sufficient mobility in the microstructure. Generally speaking, melting temperature are good indicators of diffusion rates. Materials with lower melting points have weaker atomic bonding and higher molar volumes, which allow faster diffusion at a given temperature. The sintering temperature is typically chosen greater than approximately 80% of the melting temperature to achieve wanted mass diffusion in powder mixture[59]. It's also known for Mg-Si system (figure 20), the magnesium is the moving species that diffuses into Si, so choosing magnesium as liquid phase is reasonable[60].

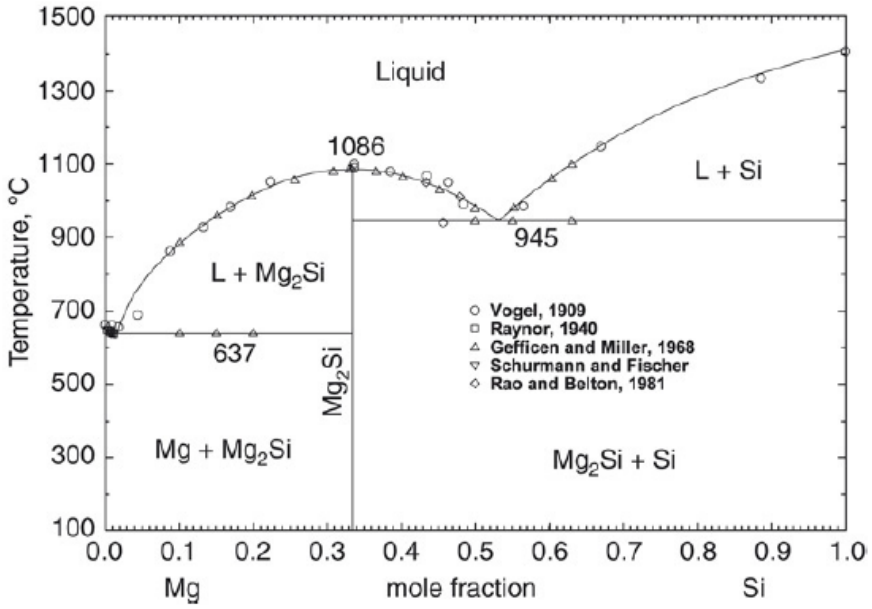

Figure 20 Optimized phase diagram of Mg-Si binary system[49]

The pure element powders are homogenously mixed of stoichiometric with designed ratio in common ball miller with 50 rpm for > 10 hours. 10 at% more magnesium powder has been added due to magnesium's easy evaporation during heat treatment. Mixed powder and milling balls are separated by mesh, then loading into graphite crucible. Such graphite crucible then is sealed with graphite foil and titanium foil in a stainless steel tube. To avoid magnesium oxidation, all of above steps are processed in glovebox with Aragon protected. The stainless steel tubes are then placed into a tube furnace (*MTI 1500 ºC tube furnace GSL-1500X*) to slow cook under vacuum condition (normally under 15 *mTorr*).

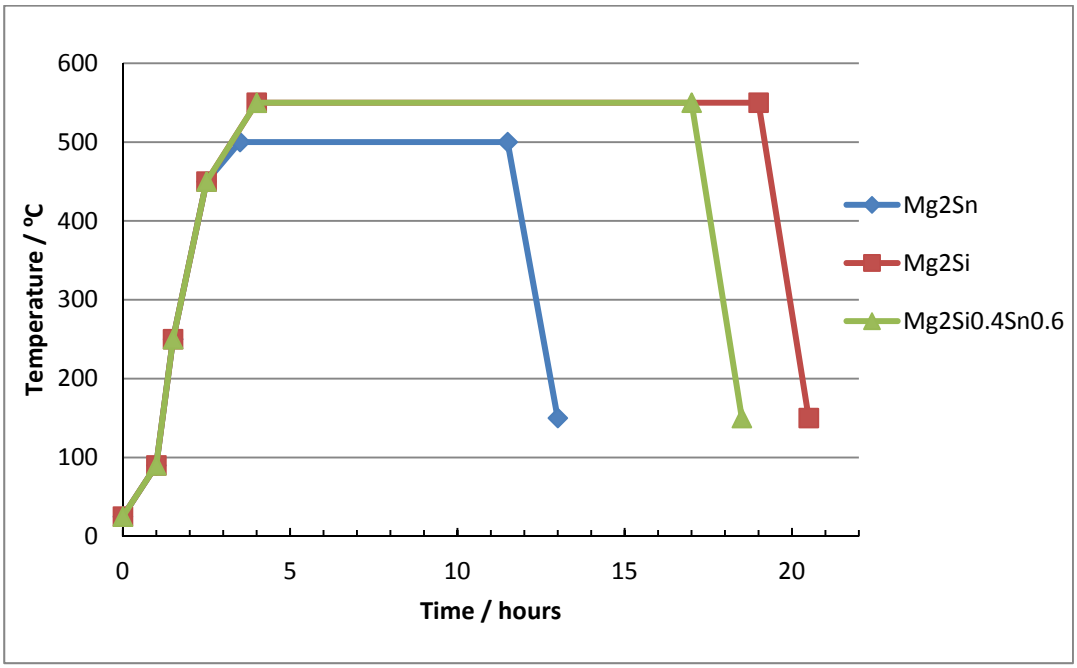

Figure 21 Temperature curves of slow cooking for Mg_2Sn & Mg_2Si

Figure 21 shows the slow cooking temperature curves as functions of time. The Mg-Si-X solid solution system follows solid state sintering mechanism due to high melting point of silicon (1440 ºC) and large difference of melting points of magnesium and silicon, thus sintering temperature 550 ºC is chosen a slightly higher than 80% of magnesium's melting point (650 ºC). In Mg-Sn-X slow cooking, 500 ºC is high enough to melt low melting point constituent tin (232 ºC), which can form the liquid phase to penetrate in magnesium powder then magnesium stannide ingots are got following liquid phase sintering theory. Titanium foils are more reactive than magnesium, so they are placed on top of powder mixture to remove oxygen and protect powders during high temperature. Graphite foils are for better sealing condition.

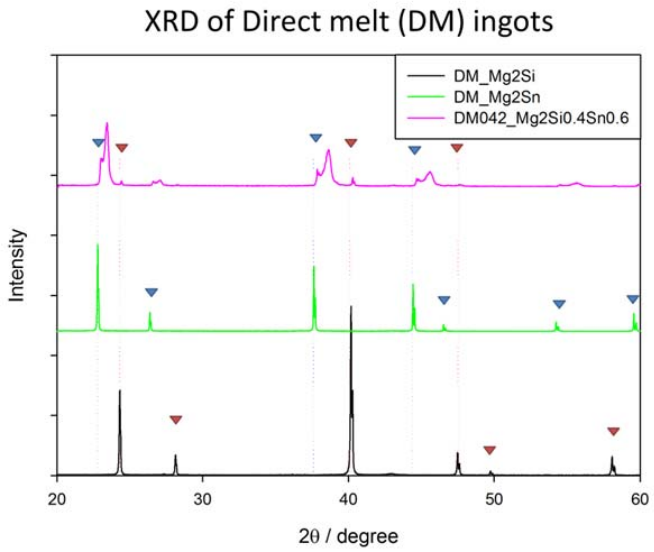

Figure 22 XRD curve of Mg_2Sn, Mg_2Si and $Mg_2Si_{0.4}Sn_{0.6}$ powder sintered by slow cooking

Figure 22 shows three typical XRD curves got from slow-cooking samples. The directional magnesium-silicon-tin powder mixture slow cooking were also tried, however, unreacted silicon peaks were observed very frequently from XRD curves. In figure 22 $Mg_2Si_{0.4}Sn_{0.6}$ XRD curve is the best result comparing to other samples. This is mainly due to too large difference of melting points among three materials. Slow cooking each solid solution has improved powder properties. The black and green curves are typical Mg_2Si and Mg_2Sn curves respectively from slow cooking. NO or very weak magnesium oxide peaks are shown in powder XRD results indicates it's an effective way to prepare doped Mg_2Si and Mg_2Sn ingots.

Achieved $Mg_2Si_{1-n}X_n$ and $Mg_2Sn_{1-m}X_m$ ingots could be easily crashed in morta and pestle. Then 0.4:0.6 mole ratio of $Mg_2Si_{1-n}X_n$: $Mg_2Sn_{1-m}X_m$ are weight and loaded into vacuum jar which is sealed by O-ring. Such vacuum jar is then mounted on clamp of high energy ball miller with 1300 rpm milling speed (*Desktop 110v High Energy*

Vibratory Ball Mill of Across International Co.) by Ø8mm stainless steel balls (volume ratio of balls and powder is ~1). After 2- 6 hours ball milling, powders sizes are widely distributed from around 100 nanometers to several micrometers. To get rid of oxidization and moisture effect of powder, both powder loading and unloading operate inside glovebox. The relation of ball milling time, ball size and particle size will discuss in detail in following section.

As mentioned before, most kinetic energy of balls movement will lost as heat during ball milling, the temperature could increase very quick especially during high energy ball milling. Air cooling is necessary for safety. The ball milling technique is ideal for brittle materials due to the constant fracturing and welding during milling. However, due to the difference of brittleness between Mg_2Si and Mg_2Sn, it's easy to get aggregation on the walls of jar and balls, which makes hardness to retrieve all powder.

2.2.2 Analysis of the powder particle size and ball milling time

Time control is important for powder preparation. On one hand, according to fig. the rate of particle size decreasing is roughly logarithmic with process time. Once the particle size enters nano-dimension, further refinement seems to be impossible[32]. On another hand, longer time means more possibilities of iron contamination introducing, aggregation growing by the random attachment of small particles in Brownian motion around the aggregate[61], as well as more powder adhered to the surface of larger particles, balls and jar walls due to high free surface energy ("Ostwald ripening").

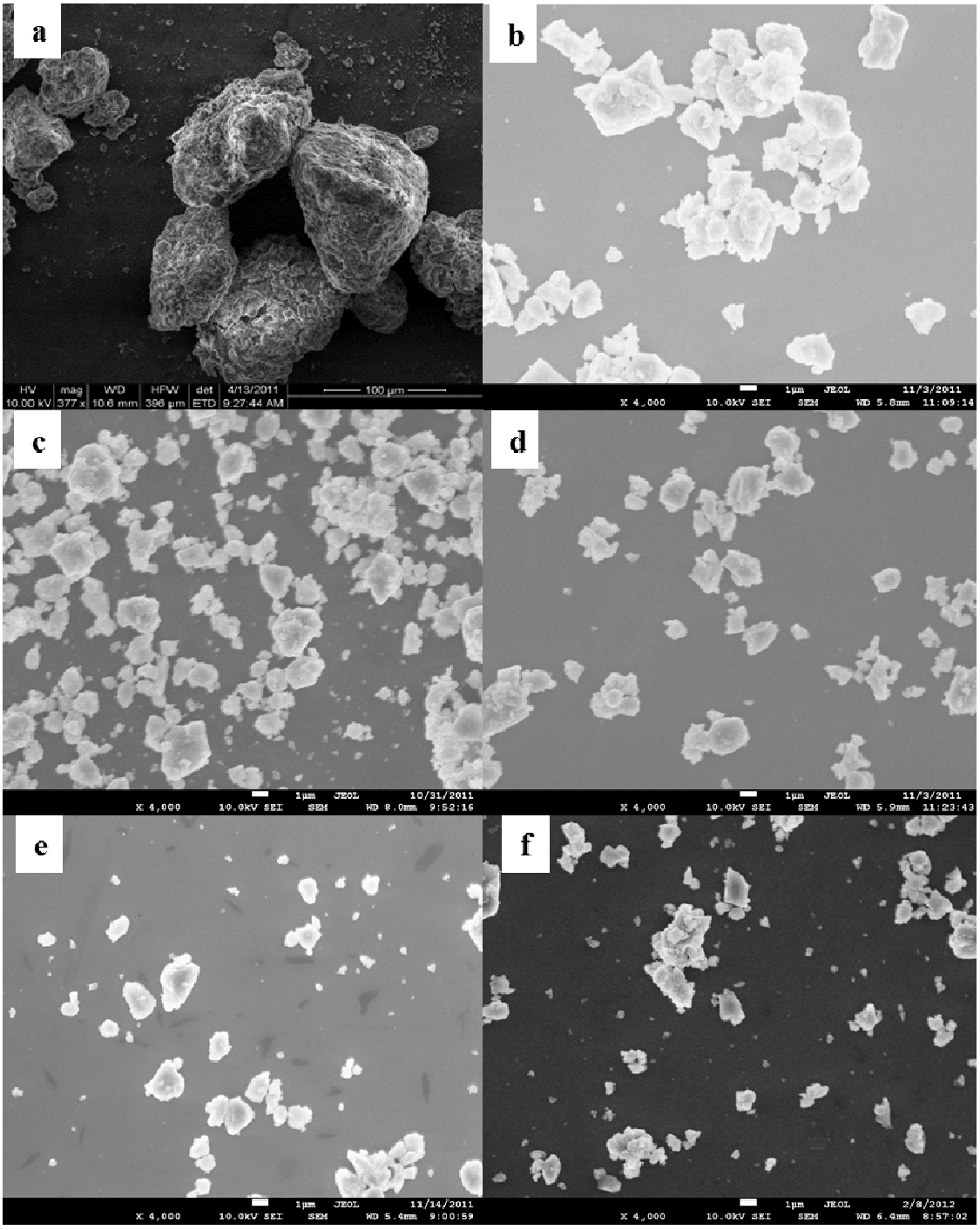

Figure 23 SEM images for ball milled powder under different conditions:
a. Common ball milling 385 hours; **b**. High energy ball milling 1hour;
c. High energy ball milling 2 hours; **d**. High energy ball milling 3 hours;
e. High energy ball milling 4 hours; **f**. High energy ball milling 6 hours.
(all high energy ball millings are by 8*Ø10mm stainless steel balls)

According to figure 10, too long ball milling time cannot result further reduced particle size, and following figure 23 and 24 have proved this phenomenon of our high energy ball milling. If ball milling time is too long, the already-achieved fine particle may aggregate together again and stick to the ball and wall, so high energy ball milling time control is important for wanted particle size. Comparing (a) to other five SEM images in figure 23, the resulting particle size of high energy ball milling (1500 rpm) is much better than that of common milling (50 rpm). As time increasing, the finest particles size drops from 10s micrometers (b) to 100s nanometers (e). There is not so much difference between (e) and (f), zoom-in images have been shown in figure 24 (b) and (c); however, there is dramatic improvement comparing to (a) 2hours ball milling. Therefore 4-6 hours ball mill time is reasonable for designed experiment condition.

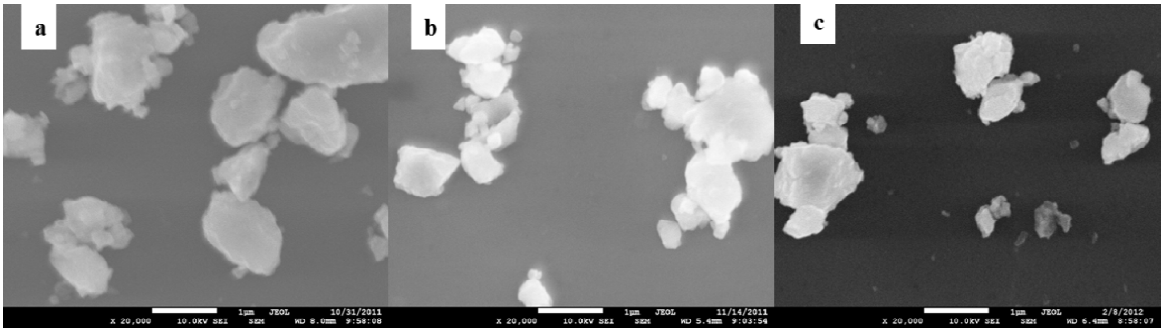

Figure 24 SEM images of high energy ball milled powder under different ball milling time:
a. 2 hours; **b**. 4 hours; **c**. 6 hours (all by 8*Ø10mm stainless steel balls)

During high energy ball milling, the impact energy from the ball bearing is readily transferred to milled materials resulting them fracture, so ball size and weight are also important factors effected final particle size. Larger balls (≥ 20mm diameter) with heavy weight are good for particles' plastic deformation but also easier lead the iron

contamination[62]; while too small ball (≤ 8mm diameter) were found to have no enough kinetic energy to diminish the bulk materials. As shown in figure 25, stainless steel ball size which is ≤ Ø6.2mm (a) is not heavy enough to get wanted particle even having a longer ball milling time (9hours) comparing to (b) and (c) (4hours). Comparing (b) (Ø10mm) and (c) (Ø12.5mm), one can find the heavier the ball, the more the fine powder are got.

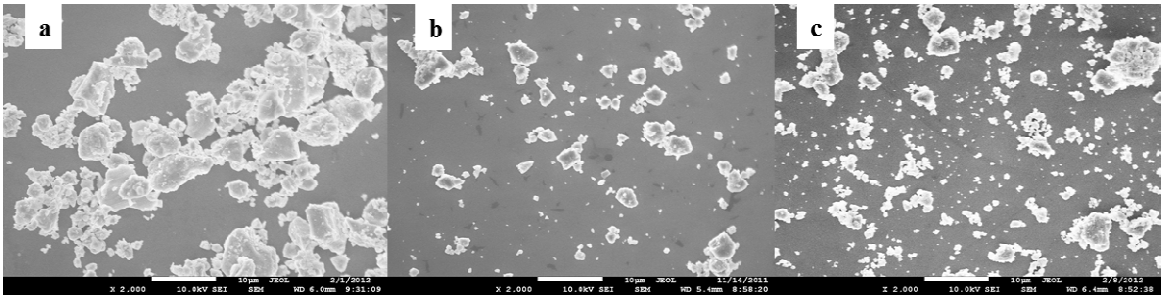

Figure 25 SEM images of high energy ball milled powder under different milling conditions:
a. 12*Ø6.2mm stainless steel balls for 9hours;
b. 8*Ø10mm stainless steel balls for 4hours;
c. 3*Ø12.5mm stainless steel balls for 4hours;

To summary, 4 to 6 hours high energy ball milling with Ø12.5 mm balls by ball-powder volume ratio ~1 is suggested ball milling condition for well-distributed particle size powder, which should be 100s' nanometers to 10s' micrometers.

2.2.3 Powder cold compaction

Magnesium silicide and magnesium stannide powder mixture got from high energy ball milling are carefully poured into 0.5" internal diameter(ID) stainless steel die cavity under Aragon protection, two punches seals the hole, the shorter one is state on bottom side and the longer one is movable. A load is then applied via the advancing punch by hydraulic hand press (*CARVER 12-ton hydraulic laboratory*) with 5.5 to 6 tons

for 25~30 minutes. During compaction, the die and bottom punch are stationary relative to daylight-level of Carver press.

There are several limits of cold press include: size restrictions due to press capacity, height-to-diameter limitation due to die wall friction, ejection cracking problems with compacts pressed from powders with poor green strength[35]. Because the applied force is fixed, sample with smaller diameter has higher pressure leading to higher green density. As a consequence of die wall fiction with punch, a density gradient occurs, with highest density area to punch face and lowest density of middle plane. That's why height-to-diameter limitation is important in cold press. The homogeneous density of sample is also important to current intensity distribution in following sintering step which directly effects the temperature distribution. Then less powder weight is especially important for more fine particles as mentioned in section 1.4.3; because the more fine the particle size, the stronger withstanding capability to pressure. Also densification is inhibited when pore sizes are large because large pores shrinkage is based on vacancy diffusion, which cannot finish in short time.

So 0.7~0.8g powder loading for at 30 minutes to get sample thickness 1.5~2.5mm is suggested here for better sintering result. If the thickness is smaller than 1.5mm, samples after DC-assisted hot pressing will be easy crack into pieces; or thickness is larger than 3mm, samples will be easy to crack across the thickness direction possibly due to it's too thick to achieve throughout pressure distribution along longitudinal direction, as said in section 1.4.3, cold pressed sample often has higher

density on surface touching with punches, then the middle plane of sample cannot be sintered as well as two sides.

There are obvious exothermic phenomena when compact pallet is getting out of die. This is possibly due to nano-size particle absorbs moisture in air. Such phenomena did not happen when powder were just after common ball milling. Full density sample from nanosize powders is achieved when green structure contains a narrow pore size distribution, i.e. a narrow distribution of ball milled particle sizes.

2.2.4 DC assisted hot press sintering procedure

Cold compacted pallets are put into graphite die with stainless steel tubing cycle to enhance the mechanical strength of die during process. Such stainless steel tube and graphite die are loose fitting at beginning because their different thermal expansion. Steel has higher thermal expansion coefficient than graphite, which leads graphite part of tight fitting easily cracks during sintering. Two thin graphite foils are cut to suitable shape and placed on bottom and top side of pallet. A little graphite powder is added between steel punch and graphite foil to protect sample from too much air contact during sintering as well as sample leakage because of too high temperature in case .

To achieve even temperature distribution in electrical current assisted sintering, homogeneity of sample density distribution is very important. External pressure is important because it strongly effects current distribution inside bulk sample, interface heat generation and heat flow across the contact interfaces. The contact resistance between sample and die cavity wall is the main cause of temperature difference development[63].

The vertical punches and sample between the two punches subjected to a uniaxial pressure are suffering an elastic deformation composed of a contraction along the longitudinal axis and an expansion along the radial direction. Contact tightness (the contact pressure **p**) in figure 26 was enhanced with increasing external due to Poisson induced deformation of punches.

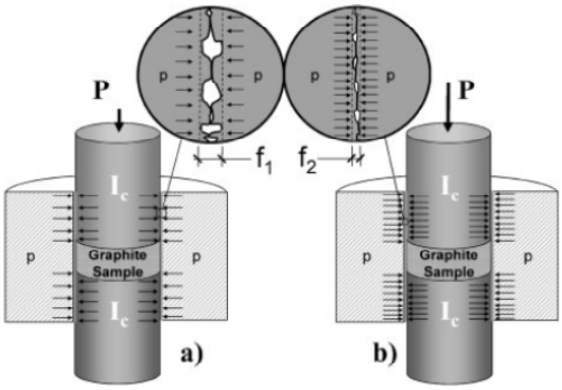

Figure 26 Two different punch/die fit configurations as a function of external pressure: a) loose and b) tighten, where Ic is the passing current[64].

Temperature differences across the punch/die/sample assembly decreased with increasing pressure, which means the applied pressure strongly controls the overall temperature distribution through the tightness condition of the punch/die contact fit[38]. However, normally use of graphite containers limits the mechanical levels to low values, generally 100 Mpa. Then the different thermal expansion coefficients of sample and graphite die make die easy to crack. To enhance the mechanical strength of die and elongate lifetime of hot-press die, stainless steel tube is placed outside of graphite die as

shown in figure 27, graphite part with 0.5” cavity and stainless steel outer part with ID 1.5”.

Figure 27 DC-assisted hot pressing die

In this thesis, the simpler current waveform constant DC is chosen, which is completely characterized by the current intensity. Application of pressure is also important. On one hand it leads decrease of sintering temperature by Joule heating due to less contact resistance; on the other hand, it hinders the grain growth then reduce final grain size.

Steel punches are chosen due to better mechanical strength especially under high temperature condition comparing to graphite punch, which is too brittle to crush when applied force is higher than 1 ton of sintering *(~114 Mpa* pressure applied on 0.5” sample). Graphite die is chosen as it’s a quite good electric contact material with high temperature oxidation resistance, good thermal/mechanical stability at high temperature and high melting point, as well as self-lubrication for easy punch loading and unloading.

Figure 28 shows the schematic diagram of DC-assisted hot pressing of this thesis. Copper plates are chosen as electrodes because of their excellent electrical conductivity; steel plates place on top and bottom side of hot press die to maintain right angle press-down during whole sintering process; graphite foils between steel plates and copper plates are to protect electrodes and more important, reduce the contact electrical resistance; graphite foils between steel plates and punches are to separate the same material in case them sintering together under high temperature and high current passing.

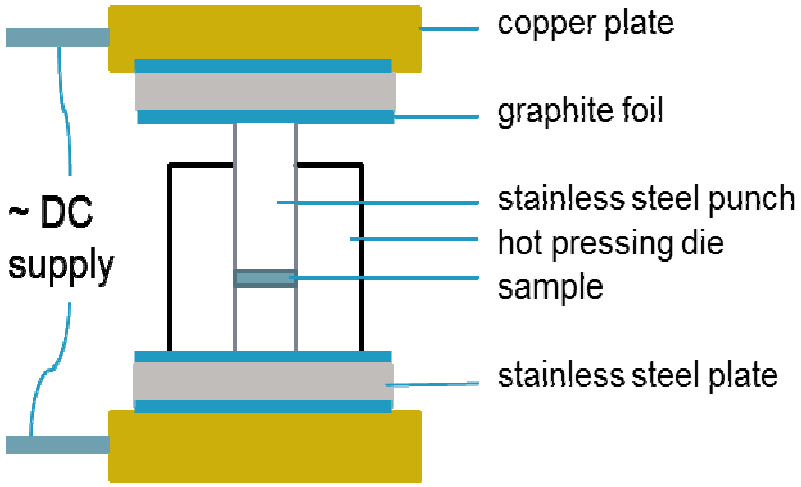

Figure 28 Schematic diagram of DC-assisted hot pressing sintering

Imperfect contacts caused by surface roughness, texture, impurities, insulating layers or oxidation, may involve complex behavior of thermal and electrical resistances at the interfaces which can be very hard to predict[38]. Normally in electrical current assisted hot press, the main contact interfaces are located between the graphite die and punches, die and samples, sample and punches. So before each sintering process, the

copper electrodes, stainless steel punches and plates were all grinded by sand paper to remove surface oxidation.

There is a minimum voltage below which preforms were not sufficiently strong[40]. Here 4v is chosen as setting voltage during sintering. Normally the reduction of voltage is around 1v during sintering process. It's hard to measure temperature correctly during sintering, so the electric current and time are important parameters to estimate temperature. Further discussion of sintering current and time's effect on micromorphology of samples' fresh fracture surface will be shown in following section 3.1.

3. MICROMORPHOLOGY AND THERMAL CONDUCTIVITY ANALYSIS

3.1 SEM Images Analysis of Sintered Samples

As shown in section 2.2.2, sintered powder's particle size widely distribute from 100~200nms to several micrometer. For submicrometer sized particles, there is no dependence of the final density on heating rate, but grain size strongly dependent on heating rate because the dominant nondensifying mechanism is grain boundary coarsening at lower temperature[65]. But for nanometric powders, an increasing heat rate resulted in a decrease in the final density because of large thermal gradients existing with high heating rates[55,66]. The temperature gradient leads outside of sample to sinter while the inside still has considerable porosity. That's why center part pieces of sample were taken for SEM images.

In this thesis, Archimedes' method[67] was used to briefly test samples' density. The theoretical density of $Mg_2Si_{0.4}Sn_{0.6}$ is 3.02 g/cm^3, and our samples' average density is 2.62~2.80 g/cm^3 which is 86.75~94.37% of theoretical density. However, there huge error introduced during test such as test liquid density change due to temperature changing during long time test and close porosity volume percentage is hard to get. That's why SEM tests are important to figure out the optimized synthesis conditions although they partly show microscopic structure information of samples.

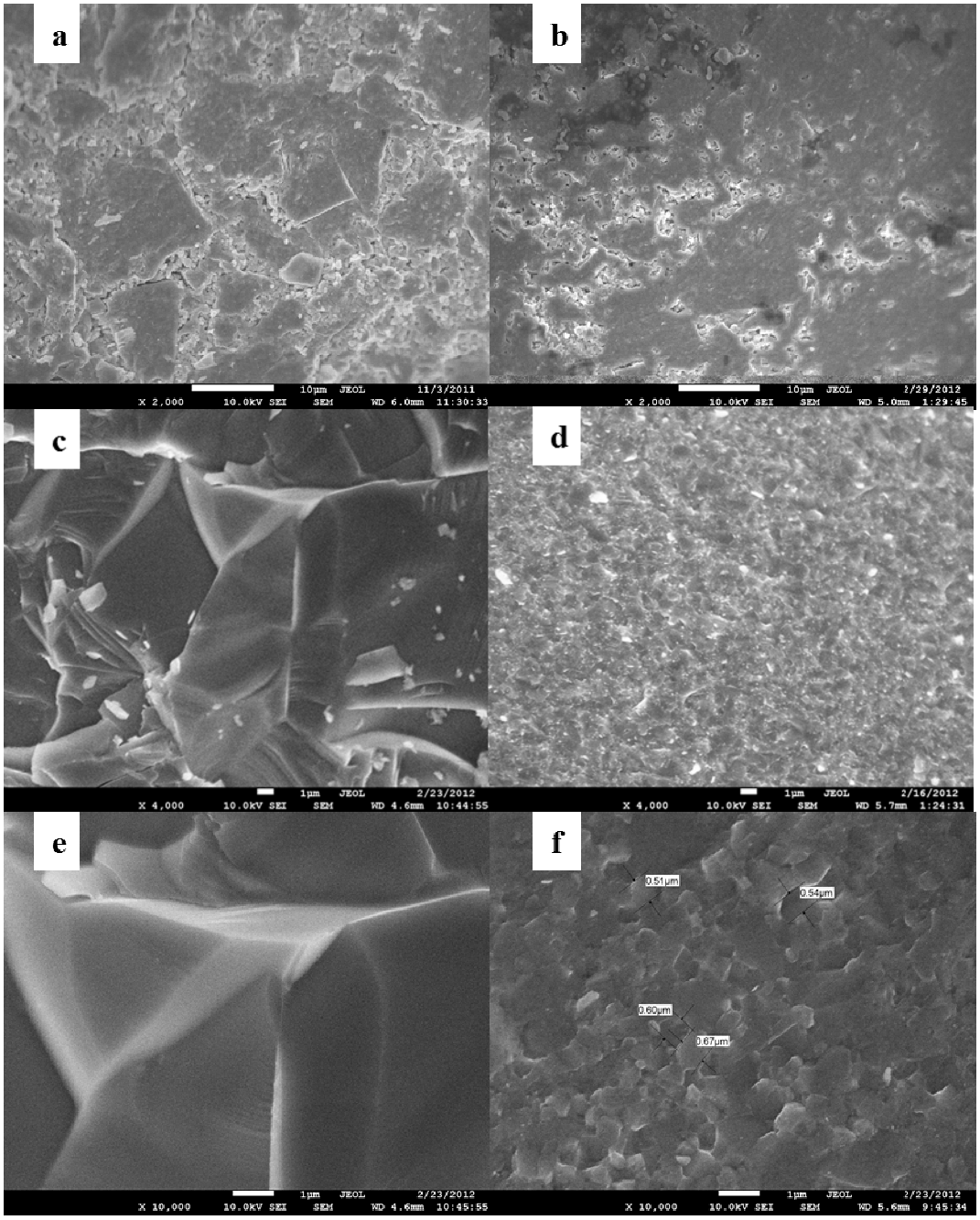

Figure 29 SEM images of sintered samples by different initial particle sizes
a. Sample **051**($Mg_2Si_{0.3925}Sn_{0.6}Sb_{0.0075}$) 600A, 45mins, high energy ball milling 1hour;
b. Sample **052**($Mg_2Si_{0.3925}Sn_{0.6}Sb_{0.0075}$) 600A, 45mins, high energy ball milling 3hours;
c. Sample **029**($Mg_2Si_{0.3925}Sn_{0.6}Sb_{0.0075}$) 800A, 70mins, common ball milling ~120hours;
d. Sample **067**($Mg_2Si_{0.375}Sn_{0.575}Bi_{0.05}$) 750A, 60mins, high energy ball milling 4hours;
e. Zoom-in image of sample **029**; f. Zoom-in image of sample **067**
(all sintering were under 2/3 ton pressure)

First, the initial powder's particle size has strong effect on final samples' microstructure. As shown in figure 28, different ball milling methods introduce different powder particle size which dramatically affects the final samples' internal porosity, comparing figure 29 (a) and (b). The only difference between Sample 029 and 067's processing conditions is ball milling way, 029's powders were from common ball milling and 067's powders were from high energy ball milling. As it has been proved by figure 23, high energy ball milling can obviously decrease the ball milled powders' particle size then decrease the final sintered samples' grain size. Comparing figure 28 (c,e) and (d, f), sample 029's grain size is tens to hundreds micrometers but 067's grain size reduces to submicrometers.

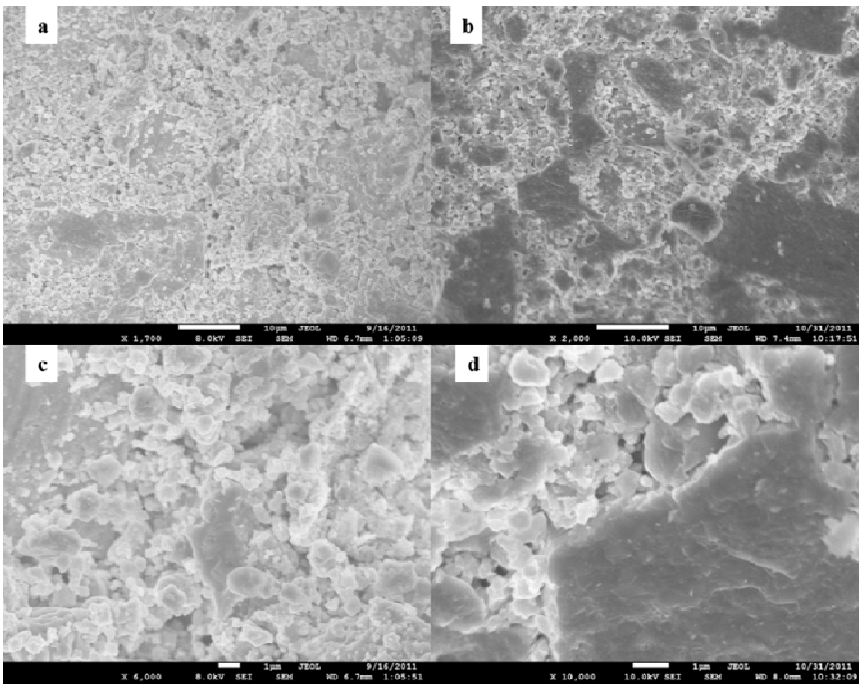

Figure 30 SEM images of sintered samples by different sintering pressures
a. Sample **044**($Mg_2Si_{0.4}Sn_{0.6}$) 700A, 30mins without pressure during sintering;
b. Sample **048**($Mg_2Si_{0.3925}Sn_{0.6}Sb_{0.0075}$) 600A, 30mins under 2/3 ton;
c. Zoom-in image of sample **044**; d. Zoom-in image of sample **048**

Second, the pressure during DC-assisted hot press sintering is also important to reduce internal porosity of samples. Comparing figure 30(a, c) and (b, d), both 0.5" samples were uniaxial cold pressed under 5.5-6 ton from 1hour high energy ball milled powder, then sintered in graphite die and stainless steel punches. One can see under the same sintering time, even sample 044 had larger sintering current but it still has much more porosity than sample 048 mostly because there was no pressure during sintering.

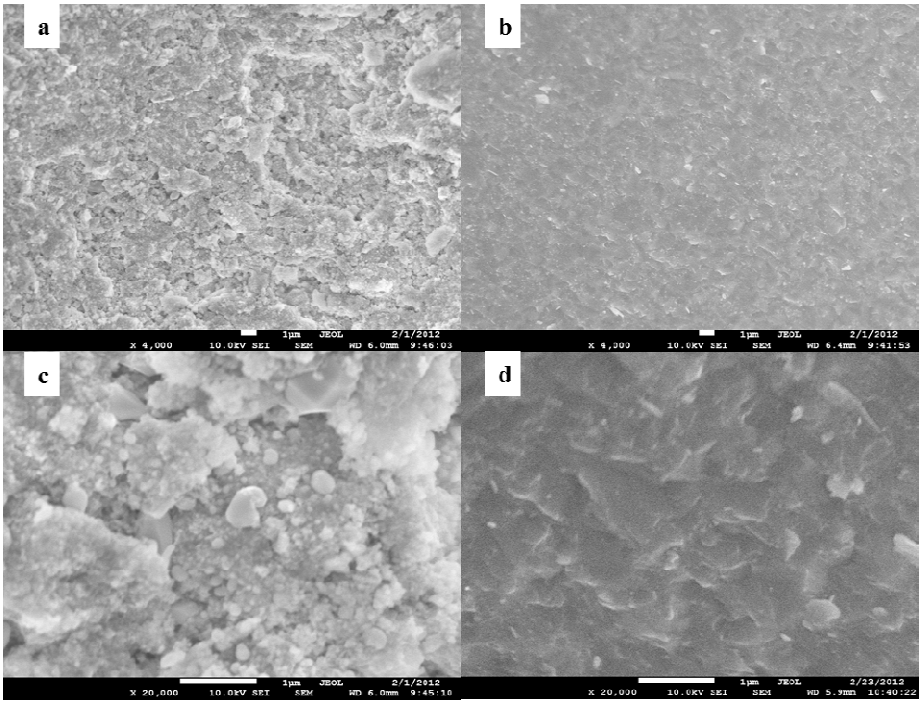

Figure 31 SEM images of sintered sample under different sintering times
a. Sample **064**($Mg_2Si_{0.35}Sn_{0.55}Sb_{0.1}$) 750A, 30mins under 2/3 ton;
b. Sample **063** ($Mg_2Si_{0.35}Sn_{0.55}Sb_{0.1}$) 750A, 60mins under 2/3 ton;
c. Zoom-in image of sample **064**; d. Zoom-in image of sample **063**
(both samples' powder were from 6hours high energy ball milling)

Third, sintering time is another important factor to control quality of samples especially for full density samples. In figure 31 the main difference between sample 063 and 064 is DC-assisted hot pressing time. The longer sintering time, the smaller internal

porosity percentage is. Meanwhile, the real-time temperature monitor of DC-assisted hot pressing is hard to achieve due to high current passing during sintering as well as high temperature makes electrical insulation and assembling of thermal couple more difficult. So electric current is considered as temperature reference, although during current rising period and cooling period temperature is hard to estimate due to very quick heating rate of joule heating by DC passing.

To summary, high energy ball milling and sintering pressure, current and time are key factors to control porosity of final samples. Further work should focus on precious density test combining with SEM test results to guarantee good samples whose density can reach the theoretical density 3 g/cm^3. 4 to 6 hours high energy ball milling with Ø12.5 mm balls by ball-powder volume ratio ~1 is suggested; around 700 Mpa pressure for no less than 25 minutes cold press is necessary for a good pallet (thickness < 3mm); sintering pressure no less than 76 Mpa is required to effectively reduce porosity volume of sample. Sintering current and time needs to be further researched to figure out an optimized combination.

3.2 Crystal Structure Analysis by X-Ray Diffraction

Three processing strategies to get Mg_2Sn-Mg_2Si solid solutions with certain doping materials have been tried, best of which was chosen as the main processing. XRD results can further show the advantage of chosen synthesis steps. To clearly explain samples' improvement, all three synthesis flow charts have been shown in figure 32. Table 4 lists Mg_2Sn-Mg_2Si solid solutions samples by different processing shown in figure 32.

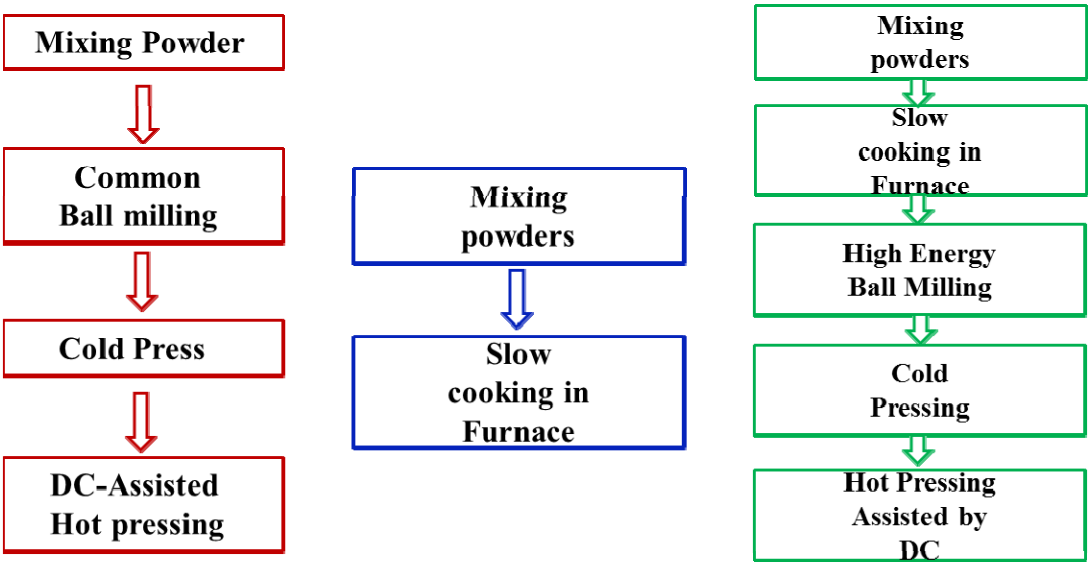

Figure 32 Synthesis strategies' development

Table 4 Sample lists of XRD results figure 34&35

Samples	Synthesis Condition
002 $Mg_2Si_{0.4}Sn_{0.6}$ **017** $Mg_2Si_{0.3925}Sn_{0.6}Sb_{0.0075}$ **029** $Mg_2Si_{0.4}Sn_{0.6}$	Common ball milling >3 days 800 A, 60-90 minutes
***DM025** $Mg_2Si_{0.4}Sn_{0.6}$ ***DM042** $Mg_2Si_{0.3925}Sn_{0.6}Sb_{0.0075}$ ***DM052** $Mg_2Si_{0.3925}Sn_{0.6}Sb_{0.0075}$	Common ball milling >3 days 550 ºC, 13 hrs under vacuum condition
046 $Mg_2Si_{0.3925}Sn_{0.6}Sb_{0.0075}$ **047** $Mg_2Si_{0.3925}Sn_{0.6}Sb_{0.0075}$ **054** $Mg_2Si_{0.3925}Sn_{0.6}Sb_{0.0075}$	High energy ball milling 1~4 hrs 600 A, 30 mins
056 $Mg_2Si_{0.3925}Sn_{0.6}Sb_{0.0075}$ **063** $Mg_2Si_{0.35}Sn_{0.55}Sb_{0.1}$ **067** $Mg_2Si_{0.375}Sn_{0.575}Bi_{0.05}$	High energy ball milling for 4hours Cold press under 6 ton for 0.5 hours

** DM samples are powder-look not bulk materials*

There are two main characteristic peak-pairs of Mg_2Sn-Mg_2Si solid solution: 2θ of one pair is 22-23º and the other is around 38º as shown in figure 33. At beginning as shown in left red flow charts of figure 32, Mg-Si-Sn with or without doping material element powder mixtures have been directly ball milled by common mill for two to three days, cold pressed then DC-assisted hot pressed. There are unreacted tin peaks and silicon peaks shown in top three curves of figure 34. When we followed the middle green flow chart in figure 32 by slow cooking element powder mixture, middle three XRD curves of figure 34 were got. Obvious Mg_2Si and Mg_2Sn peaks-emerging is shown by comparing main characteristic peak pairs. Well-merged Mg_2Si and Mg_2Sn peaks at 2θ ≈ 23º or 39º of bottom three XRD curves in figure 35 have shown that's why right green flow chart in figure 32 is finally chosen as optimized synthesis strategy, which are effective proofs of good solid solution system (also refer to figure 15).

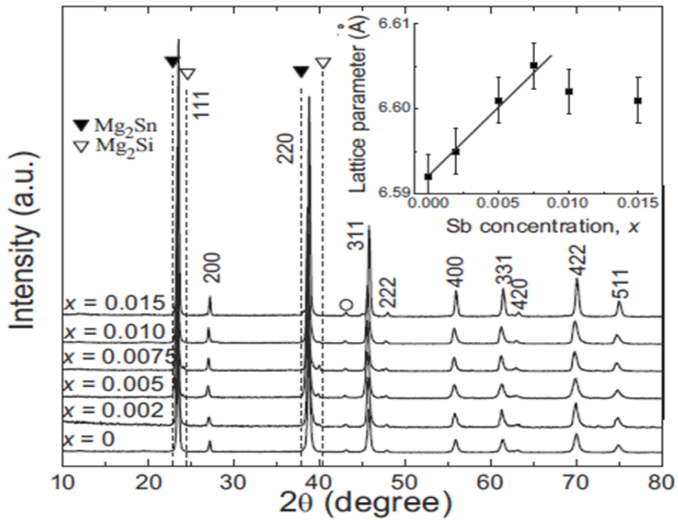

Figure 33 XRD patterns of hot-pressed $Mg_2Si_{0.4-x}Sn_{0.6}Sb_x$ samples.
The 111 and 220 peak positions for pure Mg_2Si and Mg_2Sn were indicated by dotted lines[68].

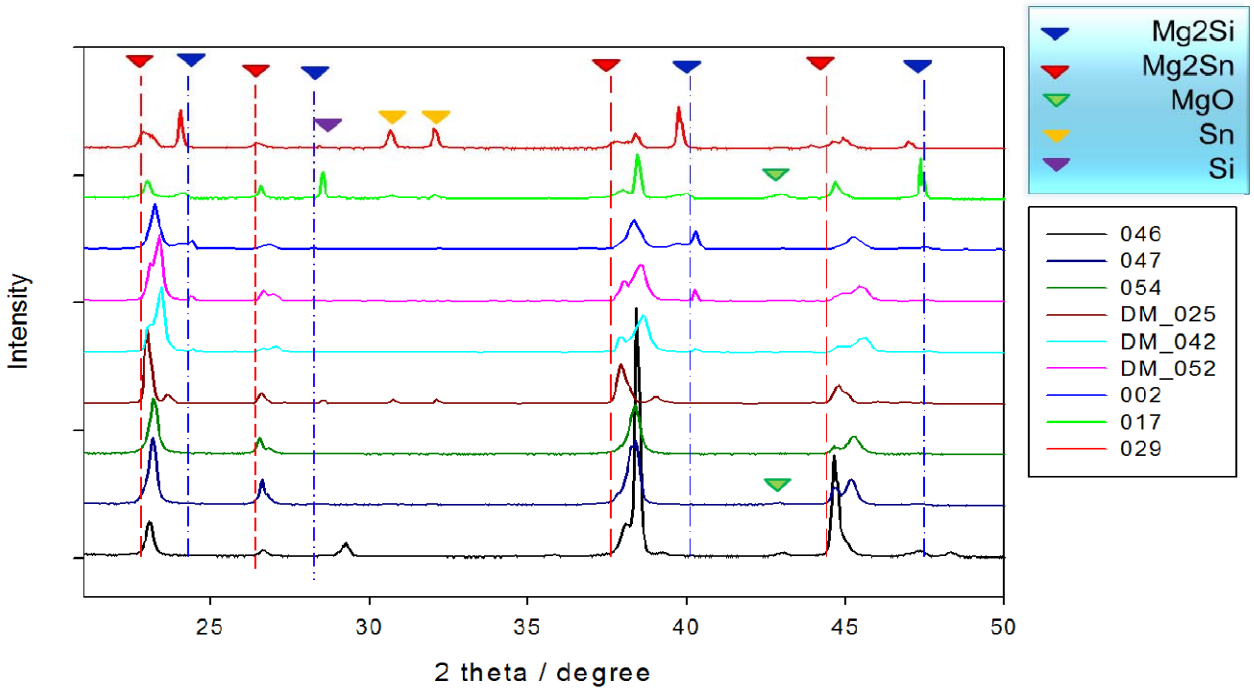

Figure 34 XRD of Mg_2Si-Mg_2Sn with antimony doped samples

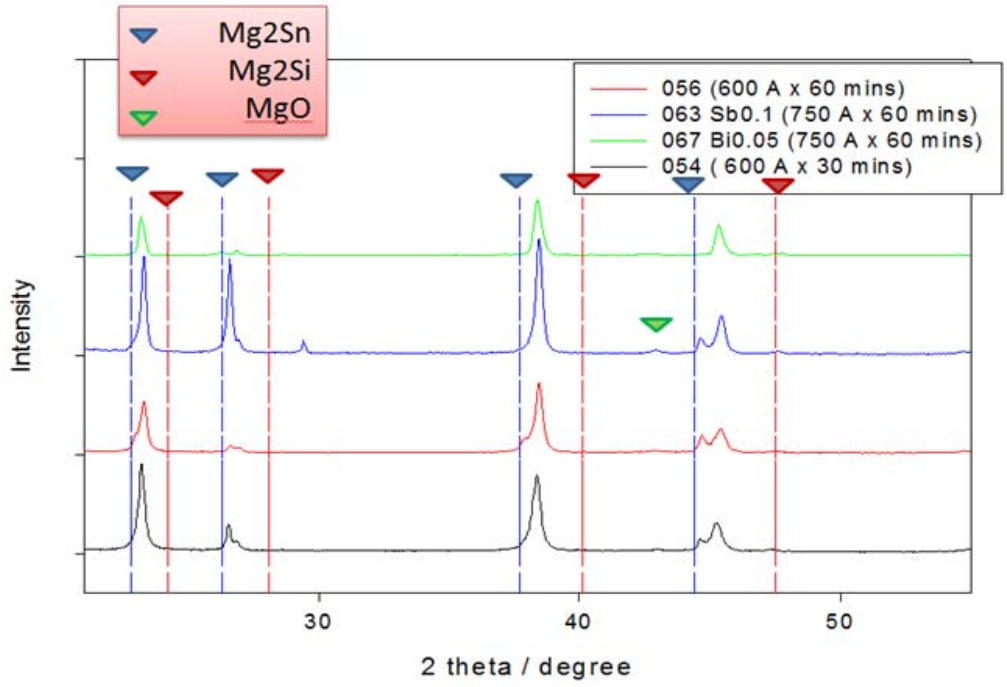

Figure 35 XRD data of Mg_2Si-Mg_2Sn with antimony or bismuth doped samples

The four samples of figure 35 have all the same processing conditions except different DC-assisted hot pressing parameters which have been briefly. There four samples are more clearly shown characteristic peaks emerging of good solid solution bulk materials. Some weak MgO peak of XRD results are acceptable, and of course there is no un-reacted silicon or tin peaks shown in bottom three XRD curves of figure 34 because separately slow cooking of doped Mg_2Si and Mg_2Sn can effectively avoid un-reacted silicon or tin due to large difference between melting points.

$$\boldsymbol{t = \frac{n \cdot \lambda_{incent}}{2 \cdot sin\theta}} \tag{8}$$

One can to estimate atomic interplanar distance $\boldsymbol{t}$ of crystalline materials by Bragg's law equation (8), where $\boldsymbol{\lambda_{incent}}$ is the wavelength of incent X-ray, normal 1542nm for copper target; $\boldsymbol{\theta}$ is Bragg angle, *i.e.* the reflection angle; $\boldsymbol{n}$ is any integer. Then one can see bismuth doping indeed change cell parameter of solid solution comparing to antimony doping by top two XRD curves of figure 35, characteristic peaks of Bi-doped sample 067 shift more left than Sb-doped sample 063 even 067's doping ratio is less than 063.

The bottom two curves of figure 35 shows the merged characteristic peaks has tendency to shift toward Mg_2Si rich area, figure 36 and 37 are the zoom-in parts of characteristic peak pair area on XRD curves. And sample synthesis conditions are listed in table 5. As shown in figure 23 (d,e), 3hours or 4hours high energy ball milling by 6.7mm stainless steel balls has not so much different particle size distribution, then only difference between 052, 053 and 054 samples is sintering time. Three different colors are used to distinguish each sample; red and blue vertical lines stand for Mg_2Sn and Mg_2Si

peaks respectively. From such interesting phenomena one could suppose longer sintering time may either enhance the Mg_2Sn phase's diffusivity to Mg_2Si phase or too long sintering may lead produced solid solution to discompose.

Table 5 Sample synthesis conditions list

Samples	Synthesis Condition
054 $Mg_2Si_{0.3925}Sn_{0.6}Sb_{0.0075}$	High energy ball milling 4 hour 600 A, 30 minutes
052 $Mg_2Si_{0.3925}Sn_{0.6}Sb_{0.0075}$	High energy ball milling 3 hour 600 A, 45 minutes
053 $Mg_2Si_{0.3925}Sn_{0.6}Sb_{0.0075}$	High energy ball milling 3 hour 600 A, 60 minutes

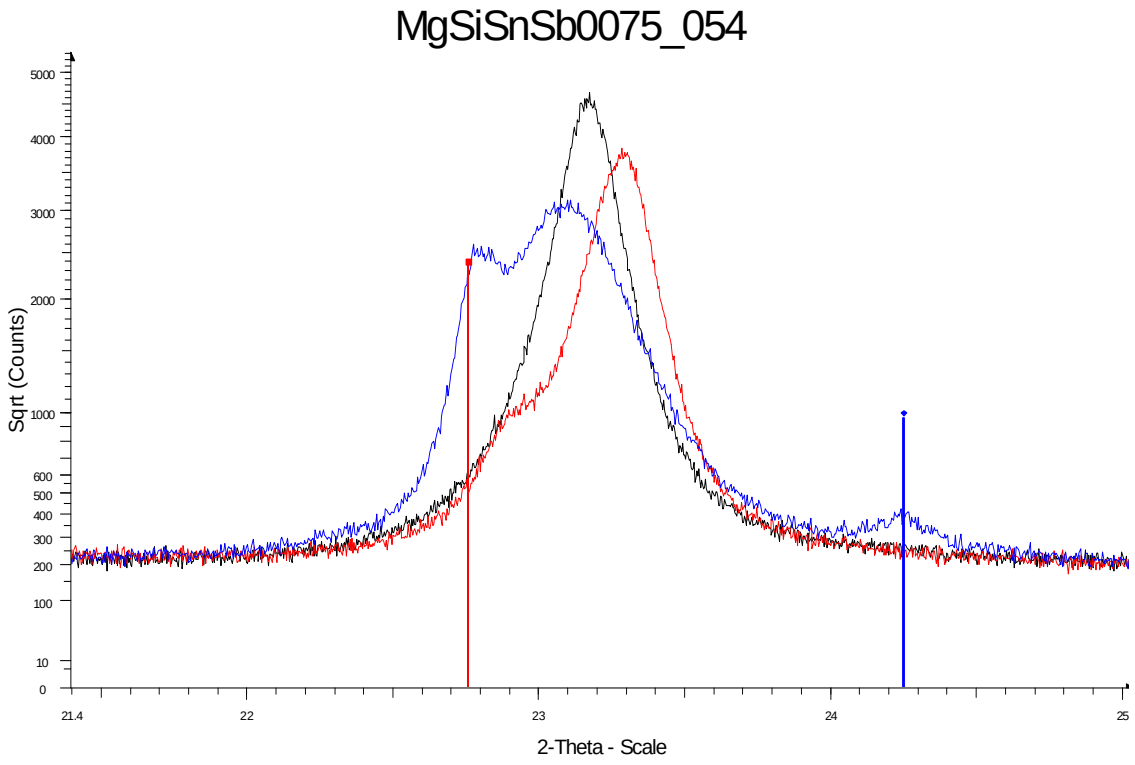

Figure 36 Characteristic peak pair near 22-23º on XRD curves of sample 052, 053, 054

However, it's very hard to get exact information of cell parameters change from comparing different doping and synthesis parameters without fixed referenced standard $Mg_2Si_{0.4}Sn_{0.6}$ or pure silicon sample in XRD tests. Because powder XRD test has large error, sometimes may even reach 0.5º which seriously affects results' analysis. One cannot judge peak shifts are by materials' self or by machine. It's kind of hard to get so-called standard $Mg_2Si_{0.4}Sn_{0.6}$ sample but further work could be carried on to get reliable judgments on doping and sintering parameters' effects.

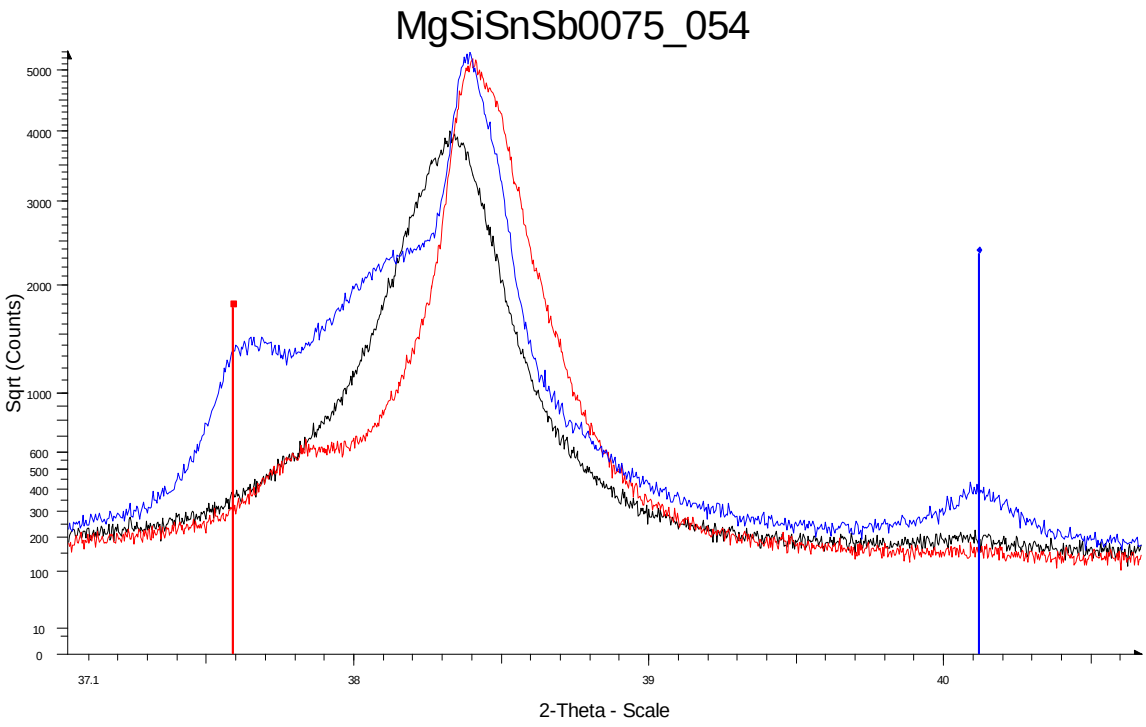

Figure 37 Characteristic peak pair near 37-40º on XRD curves of sample 052, 053, 054

3.3 Thermal Conductivity Test of Mg-Si-Sn Bulk Pallets

Three sintered samples have been test by Flash Laser methods as shown in figure 38; 002 and 007 were by *Netzsch Nanoflash LFA 447/1* and 040 was by *FlashLine 3000 Thermal Properties Analyzer*. Due to these two devices have different test temperature ranges and programings, sample 002 and 007 have a lower temperature range than sample 040 but have a higher resolution.

Samples were grinded to be less than 4 mm thickness obtained using a calliper; then one face of sample is irradiated by a short pulse laser heat, the other side's resultant temperature rising can be recorded. The infrared heated furnace chamber raises samples to designed test points. Aragon Atmosphere within the chamber is controlled to protect the samples from oxidation or other similar effects. Below the infrared furnace is the high speed pulse source, which generates light, concentrates light and feeds it into chamber right below the central sample position. Liquid nitrogen is used for cooling down InSb infrared detector. The temperature of samples under test is detected by a K-type thermoecouple located adjacent to samples and tightly contact with sample holder. Thermal conductivity can be determinated by equation (6) and (7):

$$\boldsymbol{\kappa = \alpha \cdot \rho \cdot C_p} \tag{6}$$

$$\boldsymbol{\alpha = \frac{1.38 \times d^2}{t_{1/2}}} \tag{7}$$

Here because samples are supposed to be Mg_2Si-Mg_2Sn solid solution, the heat capacity functions of magnesium silicon and magnesium stannide over temperature are got from reference[69] respectively, then specific heat $\boldsymbol{C_p}$ of sample is calculated from.:

$$\boldsymbol{C_{p_{solid\ solution}} = C_{p_{Mg2Si}} \times 40\% + C_{p_{Mg2Sn}} \times 60\%} \tag{8}$$

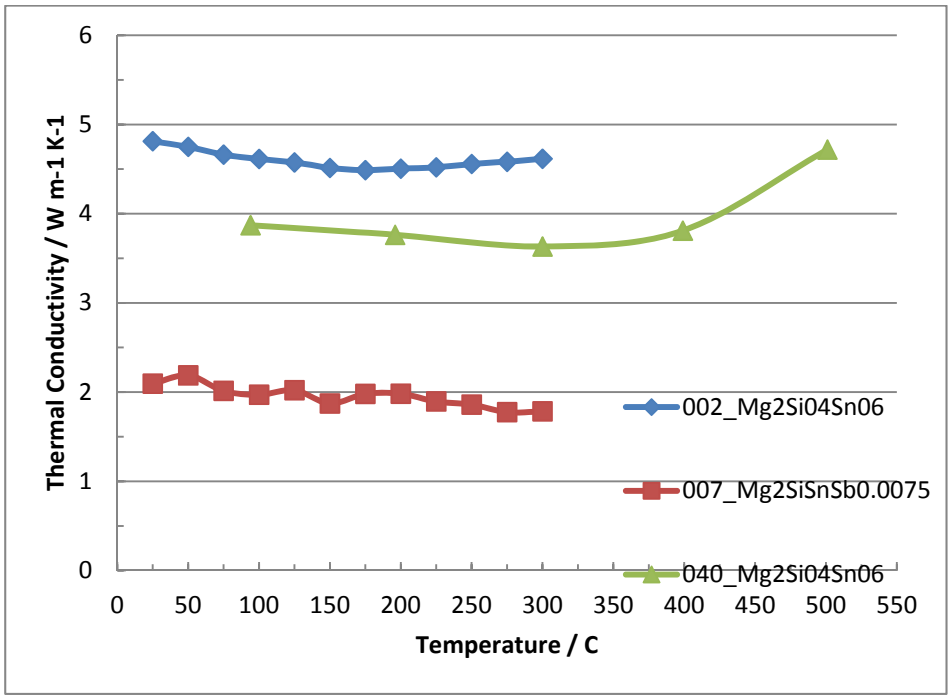

Figure 38 Thermal conductivity test results by Flash method

As mentioned before, the Flash test's results are strongly related to samples' homogeneousness, *i.e.* density distribution. The density of three samples is around 2.65 g/cm^3, which is 87.7% of calculated theoretical density 3.02 g/cm^3. Sintering conditions of these three samples are shown in table 6. But sample 040's powder preparation is under Aragon protected atmosphere. As shown in figure 39, due to porosity existing inside of sample 007, thermal conductivity reducing in figure 38 is unclear. Both internal porosities and doping antimony could introduce more phonon scattering than decrease thermal conductivity. As sample 040 was from high energy ball milled powder although it had shorter sintering time and lower sintering current, it's reasonable to suspect that sample 040 has more fine grain size than 002, which leads relative lower thermal conductivity curve than sample 002 in figure 38.

Table 6 Sample list of figure 38

Samples	Synthesis Condition
002 $Mg_2Si_{0.4}Sn_{0.6}$	Common ball milling >150 days 800 A, 90 minutes
007 $Mg_2Si_{0.3925}Sn_{0.6}Sb_{0.0075}$	High energy ball milling 1 hour 700 A, 60 minutes
040 $Mg_2Si_{0.4}Sn_{0.6}$	

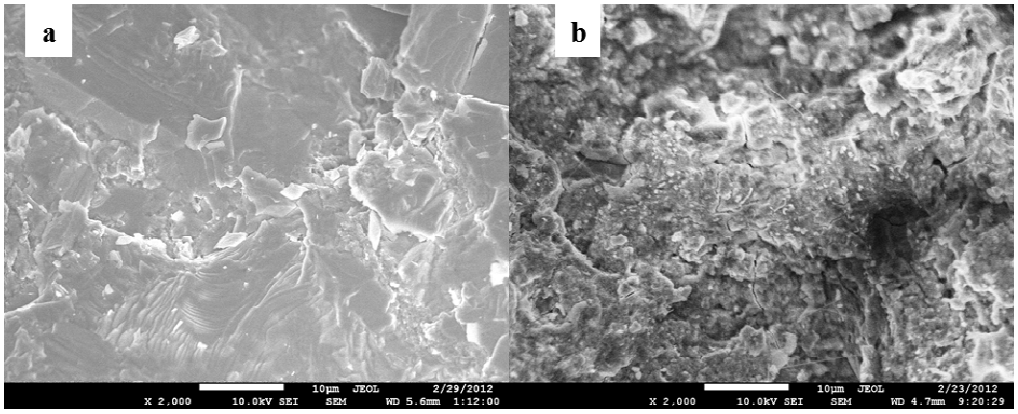

Figure 39 SEM images of **a.** 002, **b**. 007 sample

Some samples were measured by steady-state method. To get a large diameter thickness ratio, samples were grinded into thinner than 2mm. The thickness of the specimen is obtained using a calliper. The specimen is then placed between stainless steel rods. Thermal paste is applied on both sides of sample to reduce the thermal resistance between rods and samples. The bars are arranged vertically with an electrical heater, at the top end of the upper bar, situated under four copper plates on which weights are placed to make the contact resistance as uniform as possible. The upper brass part was maintained at 50 C controlled by Omega temperature controller, and the lower part at 0 C by water and ice mixture. The time for a single specimen to reach

equilibrium is usually in excess of four hours. The temperature at eight points which are distribute even on stainless steel rods are obtained and recorded by *Keithley Model 2000*. Testing is under ASTM E1530 – 06 Standard Test Method for Evaluating the Resistance to Thermal Transmission of Materials by the Guarded Heat Flow Meter Technique.

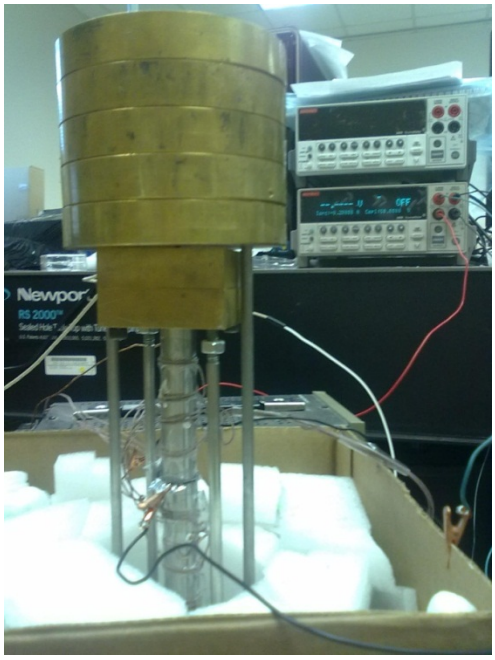

Figure 40 Steady-state thermal conductivity measurement set-up

In steady-state test (as shown in figure 40) the heat supply rate can be supposed to be at constant rate. Such set up is very flexible in operation; however, large errors will cause by radiation and heat conduction with atmosphere. The bar's conductivity should be two orders higher than test samples[70] for better test results. Equations (10-12) show how one can calculate the upper and lower temperatures gradients, then heat transfer rate q_{ave} can be calculated and upper and lower contact points' temperatures can be estimate from linear line:

$$q_1 = \kappa_{ss\,rod} \times A_{ss\,rod} \times (\frac{\Delta T}{\Delta x})_{upper} \quad (10)$$

$$q_2 = \kappa_{ss\,rod} \times A_{ss\,rod} \times (\frac{\Delta T}{\Delta x})_{lower} \quad (11)$$

$$q_{avg} = \frac{q_1+q_2}{2} \quad (12)$$

Where $\kappa_{ss\,rod}$= 17 W/m K^{-1} is the thermal conductivity of stainless steel rod, and Ass rod is area of stainless steel rod. ΔT/Δx is temperature gradients of the upper and lower stainless steel rods. ΔT can be obtained by $\Delta T = T1 - T2$.

Finally, thermal conductivity of sample can be obtained using equation (13):

$$\kappa = \frac{q_{avg} \times thickness\ of\ sample}{[A_{ss\,rod} \times (\Delta T_{sample} - \Delta T_{paste})]} \quad (13)$$

In RM temperature test, temperature of top heater was controlled around 50 □C and bottom side was cooling by ice-water mixture to keep 0 □C, it took over 5 hours to get stable temperature distribution from top to bottom along stainless steel rods across test sample. The thermal conductivity of sample 069 is 2.068 W/m K^{-1} at RT, which is comparable to literature data. Figure 41 shows the data collected from steady state thermal conductivity test of sample 069. However, its correction cannot be guarantee due to following discussion.

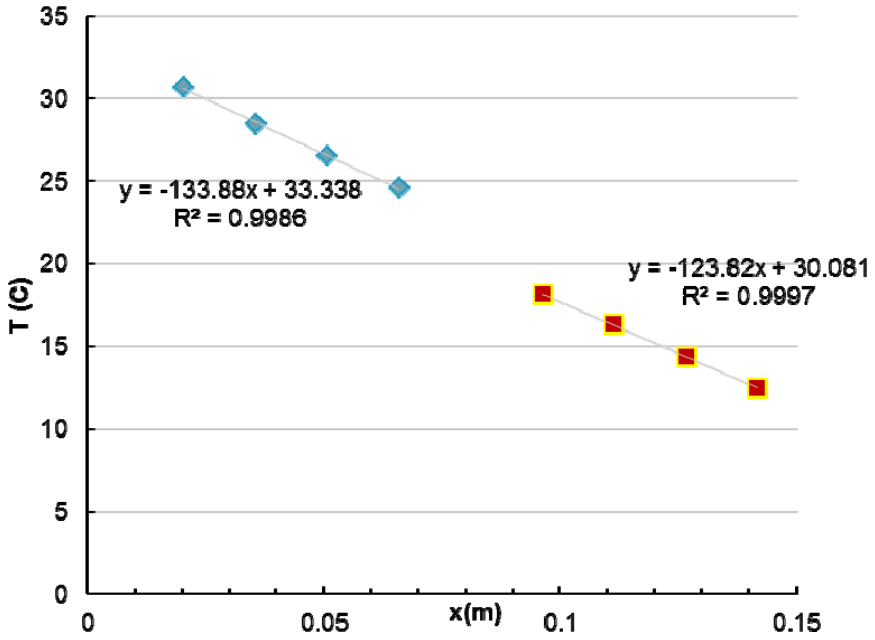

Figure 41 Typical test curve for temperature gradient of sample 069 $Mg_2Si_{0.375}Sn_{0.575}Bi_{0.05}$

Due to the low conductivity of test material, it's easy to build up an appreciable temperature gradient across even a thin sample without asking too much from the heater. Just increase powder will rapid run into trouble with increased energy losses, so time to equilibrium is long. The longer the running time was, the larger heat losses was. The heat losses due to conduct with environment atmosphere have been eliminated entirely in this test. Thus large error is hard to be avoided which leads precision of test cannot guarantee.

4. CONCLUSION AND FUTURE WORK

In this thesis, synthesis steps and thermal conductivity of antimony and bismuth doped magnesium-silicide and magnesium-stannide solid solution system have been studied. According to dimensionless figure of merit ***ZT*** value ($ZT=S^2\sigma T/\kappa$), to get better ZT value of solid solution bulk material, this thesis is aiming to show phonon's part thermal conductivity is reduced by increasing phonon scattering centers through doping materials and increasing fine grains. To gain 10s nm to 100s μm well distributed powder particles, 4 to 6 hours high energy ball milling should be by Ø12.5mm stainless still balls with powder-to-ball volume ratio ~1. Around 700 Mpa pressure for no less than 25 minutes cold press is necessary for 2-3mm thickness pallet. Sintering pressure no less than 76 Mpa is required to effectively reduce internal porosity. However, sintering current and time needs to be further researched to figure out an optimized combination to get 95% or higher density bulk Mg_2(Si, Sn) solid solution samples with fine grain size (several hundred nanometers). In Satyala et. al's[71] most recent paper, they have shown that 20 nm crystalline grain would not be beneficial to achieve higher figure-of-merit due to large electrical carrier mobility loss at grain boundaries in Mg_2Si nano-structured bulk materials. Then the design of well distributed grain size from 10s nm to 100s μm should be considered in future work.

According to well merged characteristic peaks of XRD results comparing to other two synthesis ways, slow cooking doped Mg_2Si and Mg_2Sn from element powders separately plus DC-assisted hot press can dramatically improve these two phases' well

solution. However due to huge error of powder XRD machine itself, it's hard to judge peak shift by which factor, different doping condition or synthesis parameters. Standard $Mg_2Si_{0.4}Sn_{0.6}$ sample or single crystal silicon should be used in future XRD tests as reference sample to correctly point out peaks shift. There are already some papers[48,72] pointing out cubic cell parameter of $Mg_2Si_{0.4}Sn_{0.6}$ is around 0.66nm under 600 ºC, which are very useful for doping design. Interesting peak separation of samples by different sintering time is also discussed, which needs more comparing sintered sample to prove time control is important in case of solid solution discomposing.

Antimony doping reducing thermal conductivity tested by flash method cannot be addressed due to internal porosities could also decrease thermal conductivity by phonon scattering. The steady-state thermal conductivity test of half inch sample at RT has shown comparable to flash method result. The precise density test, heat capacity of samples over temperature range by DSC and well insulation establishing during steady-state test could be considered as following work.

It's kind of regretful that electrical conductivity as well as Seebeck coefficient of samples could not be done in this study. Seebeck coefficient and resistance measurement for thin pallet samples[73] has been reported most recently which may bring huge convenience to cycle shaped samples. Because Mg-Si-Sn based bulk material is relatively brittle and kind of hard to be diced into wanted size. Directly ZT value test[74] according to transient Harman technique has been carried on by my partner, whose benefit is to eliminate multi-test and calculation errors of ZT value; but the solution of large contact resistance between test wire and sample is still under probing.

REFERENCES

[1] Mildred S. Dresselhaus, Gang Chen, Ming Y. Tang, Ronggui Yang, Hohyun Lee, Dezhi Wang, Zhifeng Ren, Jean-Pierre Fleurial, and Pawan Gogna, Adv. Mater. **19**, 1043 (2007).

[2] A. J. Minnich, M. S. Dresselhaus, Z. F. Ren, and G. Chen, Energy Environ. Sci. **2**, 466 (2009).

[3] Kajikawa Takenobu, *Thermoelectrics Handbook* (CRC Press, Boulder, Colorado, 2005), pp. 50.

[4] G. Jeffrey Snyder and Eric S. Toberer, Nat Mater **7** (2), 105 (2008).

[5] Charles Kittel, *Introduction to solid state physics*, 6th ed. (Wiley, New York, 1986), p.646.

[6] Hiroshikawamoto, Science & Technology Trends (2008).

[7] Bed Poudel, Qing Hao, Yi Ma, Yucheng Lan, Austin Minnich, Bo Yu, Xiao Yan, Dezhi Wang, Andrew Muto, Daryoosh Vashaee, Xiaoyuan Chen, Junming Liu, Mildred S. Dresselhaus, Gang Chen, and Zhifeng Ren, Science (Washington, DC, U. S.) **320**, 634 (2008).

[8] Yi Ma, Qing Hao, Bed Poudel, Yucheng Lan, Bo Yu, Dezhi Wang, Gang Chen, and Zhifeng Ren, Nano Lett. **8**, 2580 (2008).

[9] V. K. Zaitsev, M. I. Fedorov, E. A. Gurieva, I. S. Eremin, P. P. Konstantinov, A. Yu Samunin, and M. V. Vedernikov, Int. Conf. Thermoelectr. **24th**, 189 (2005).

[10] Yang Jihui, Caillat, and G. Thierry, (Materials Research Society, Warrendale, PA, ETATS-UNIS, 2006), Vol. 31, p. 6.

[11] Liangfu Lou, *Introduction to Phonons & Electrons*. (World Scientific, Hackensack, NJ, 2003)pp.xiii.

[12] "Phonon", http://en.wikipedia.org/wiki/Phonon (2011)

[13] G. H. Zhu, H. Lee, Y. C. Lan, X. W. Wang, G. Joshi, D. Z. Wang, J. Yang, D. Vashaee, H. Guilbert, A. Pillitteri, M. S. Dresselhaus, G. Chen, and Z. F. Ren, Phys. Rev. Lett. **102**, 196803/1 (2009).

[14] Ronald Phillip Tye, *Thermal Conductivity*. (Academic P. , London, New York, 1969).

[15] P. Gaal, M. A. Thermitus, and Daniela Stroe, Journal of Thermal Analysis and Calorimetry **78** (1), 185 (2004).

[16] Marsha A. Presley and Philip R. Christensen, J. Geophys. Res. **102** (E3), 6535 (1997).

[17] W. J. Parker, R. J. Jenkins, C. P. Butler, and G. L. Abbott, Journal of Applied Physics **32** (9), 1679 (1961).

[18] "Thermal Diffusivity of Flash Method", http://www.anter.com/technotes/TPN-68%20Thermal%20Diffusivity%20by%20the%20Flash%20Method.pdf (2012)

[19] L. D. Hicks and M. S. Dresselhaus, Phys. Rev. B: Condens. Matter **47**, 16631 (1993).

[20] D. M. Rowe and V. S. Shukla, Journal of Applied Physics **52** (12), 7421 (1981).

[21] Allon I. Hochbaum, Renkun Chen, Raul Diaz Delgado, Wenjie Liang, Erik C. Garnett, Mark Najarian, Arun Majumdar, and Peidong Yang, Nature (London, U. K.) **451**, 163 (2008).

[22] Y. S. Ju and K. E. Goodson, Applied Physics Letters **74** (20), 3005 (1999).

[23] Rama Venkatasubramanian, Edward Slivola, Thomas Colpitts, and Brooks O'Quinn, Nature (London, U. K.) **413**, 597 (2001).

[24] Giri Joshi, Hohyun Lee, Yucheng Lan, Xiaowei Wang, Gaohua Zhu, Dezhi Wang, Ryan W. Gould, Diana C. Cuff, Ming Y. Tang, Mildred S. Dresselhaus, Gang Chen, and Zhifeng Ren, Nano Lett. **8**, 4670 (2008).

[25] Kuei Fang Hsu, Sim Loo, Fu Guo, Wei Chen, Jeffrey S. Dyck, Ctirad Uher, Tim Hogan, E. K. Polychroniadis, and Mercouri G. Kanatzidis, Science (Washington, DC, U. S.) **303**, 818 (2004).

[26] E. Paul DeGarmo, Black, J. Temple.Kohser, Ronald A., *DeGarmo's materials and processes in manufacturing*, 10th ed. ed. (Wiley, c2008., Hoboken, NJ, 2008), pp.xvi.

[27] "Why Powder Metallurgy?" http://www.ipmd.net/Introduction_to_powder_metallurgy/Why_Powder_Metallurgy (2010)

[28] "Powder Metallurgy Powders & Equipment Manufactures" http://www.epma.com/New_non_members/pdf/2009_EPMA_Member_Guide_Powder_Equip.pdf (2009)

[29] Oh-Hun Kwon, in *Materials Science and Technology* (Wiley-VCH Verlag GmbH & Co. New York, 2006).

[30] P. W. Voorhees, Journal of Statistical Physics **38** (1), 231 (1985).

[31] D. Basset, P. Matteazzi, and F. Miani, Materials Science and Engineering: A **168** (2), 149 (1993); C. C. Koch and Y. S. Cho, Nanostructured Materials **1** (3), 207 (1992).

[32] H. Fecht, E. Hellstern, Z. Fu, and W. Johnson, Metallurgical and Materials Transactions A **21** (9), 2333 (1990).

[33] Suryanarayana C, Progress in Materials Science **46** (1-2), 1 (2001).

[34] "Attritor Grinding and Dispersing Equipment" http://www.unionprocess.com/tech_papers/ups_b.pdf (1999)

[35] A. S. M. International Handbook Committee, (ASM International, Phoenix, Arizona).

[36] "Pressing & Demoulding Method" http://www.mtixtl.com/images/Pressing%20method.jpg (2009)

[37] Carl C. Koch, (William Andrew Publishing, Burlington, MA, 2007).

[38] Gutmanas Elazar Y, Progress in Materials Science **34** (4), 261 (1990).

[39] V. Leshchinsky, R. Popovitz-Biro, K. Gartsman, R. Rosentsveig, Yu Rosenberg, R. Tenne, and L. Rapoport, Journal of Materials Science **39** (13), 4119 (2004).

[40] Roberto Orrù, Roberta Licheri, Antonio Mario Locci, Alberto Cincotti, and Giacomo Cao, Materials Science and Engineering: R: Reports **63** (4-6), 127 (2009).

[41] W. Chen, U. Anselmi-Tamburini, J. E. Garay, J. R. Groza, and Z. A. Munir, Materials Science and Engineering A **394** (1-2), 132 (2005); U. Anselmi-Tamburini, S. Gennari, J. E. Garay, and Z. A. Munir, Materials Science and Engineering A **394** (1-2), 139 (2005).

[42] "Magnesium Silicide Crystal Structure" http://www.springermaterials.com/docs/info/10681727_102.html (2011)

[43] M. Fedorov, V. Zaitsev, F. Solomkin, and M. Vedernikov, Technical Physics Letters **23** (8), 602 (1997).

[44] Y. Q. Cao and et al., Journal of Physics D: Applied Physics **42** (1), 015406 (2009).

[45] V. K. Zaitsev, M. I. Fedorov, E. A. Gurieva, I. S. Eremin, P. P. Konstantinov, A. Yu Samunin, and M. V. Vedernikov, Physical Review B **74** (4), 045207 (2006).

[46] Mikhail I. Fedorov and Vladimir K. Zaitsev, Int. Conf. Thermoelectr. **19th**, Cardiff, UK, (2000).

[47] V. Zaitsev, in *Thermoelectrics Handbook* (CRC Press, Boulder, Colorado, 2005), pp. 29.

[48] E. N. Nikitin, E. N. Tkalenko, V. K. Zaitsev, A. I. Zaslavskii, and A. K. Kuznetsov, Izv. Akad. Nauk SSSR, Neorg. Mater. **4**, 1902 (1968).

[49] In-Ho Jung, Dae-Hoon Kang, Woo-Jin Park, Nack J. Kim, and SangHo Ahn, Calphad **31** (2), 192 (2007).

[50] Sergey V. Faleev and François Léonard, Physical Review B **77** (21), 214304 (2008).

[51] Tie-Jun Zhu, Yi-Qi Cao, Qian Zhang, and Xin-Bing Zhao, Journal of Electronic Materials **39** (9), 1990 (2010).

[52] ZHANG, #160, Q., HE, J., ZHU, T. J., S. N., ZHAO, X. B., TRITT, and T. M., *High figures of merit and natural nanostructures in $Mg_2Si_{0.4}Sn_{0.6}$ based thermoelectric materials*. (American Institute of Physics, Melville, NY, 2008).

[53] Q. Zhang, T. J. Zhu, A. J. Zhou, H. Yin, and X. B. Zhao, Phys. Scr., T **T129**, 123 (2007).

[54] D E Clark and W H Sutton, Annual Review of Materials Science **26** (1), 299 (1996).

[55] Z. Munir, U. Anselmi-Tamburini, and M. Ohyanagi, Journal of Materials Science **41** (3), 763 (2006).

[56] Okazaki Kenji, Materials Science and Engineering: A **287** (2), 189 (2000).

[57] W. D. Kingery and M. D. Narasimhan, Journal of Applied Physics **30** (3), 307 (1959).

[58] R. M. German, S. Farooq, and C. M. Kipphut, Materials Science and Engineering: A **105–106, Part 1** (0), 215 (1988).

[59] Zhigang Zak Fang, (Woodhead Publishing, Cambridge, UK, 2010), p. 524.

[60] W. K. Chu, S. S. Lau, J. W. Mayer, H. Müller, and K. N. Tu, Thin Solid Films **25** (2), 393 (1975).

[61] George Y. Onoda and John Toner, Journal of the American Ceramic Society **69** (11), C (1986).

[62] J. Schilz, M. Riffel, K. Pixius, and H. J. Meyer, Powder Technology **105** (1–3), 149 (1999).

[63] Antonios Zavaliangos, Jing Zhang, Martin Krammer, and Joanna R. Groza, Materials Science and Engineering: A **379** (1–2), 218 (2004).

[64] S. Grasso, Y. Sakka, and G. Maizza, Materials Transactions **50** (8), 2111 (2009).

[65] Zuhair A. Munir, Dat V. Quach, and Manshi Ohyanagi, J. Am. Ceram. Soc. **94**, 1 (2010).

[66] Da-Jiang Chen and Merrilea J. Mayo, Journal of the American Ceramic Society **79** (4), 906 (1996).

[67] Standard Test Method for Bulk Density (Unit Density) & voids in aggregate. ASTM Standard C29/C29M-09. Vol 04.02 American Society for Testing and Materials. West Conshohocken. PA.

[68] Q. Zhang, H. Yin, X. B. Zhao, J. He, X. H. Ji, T. J. Zhu, and T. M. Tritt, physica status solidi (a) **205** (7), 1657 (2008).

[69] H. Y. Chen, N. Savvides, T. Dasgupta, C. Stiewe, and E. Mueller, Phys. Status Solidi A **207**, 2523 (2010); Benhai Yu, Dong Chen, Qingbin Tang, Chunlei Wang, and Deheng Shi, Journal of Physics and Chemistry of Solids **71** (5), 758 (2010).

[70] A. Beck, Journal of Scientific Instruments **34** (5), 186 (1957).

[71] Nikhil Satyala and Daryoosh Vashaee, Applied Physics Letters **100** (7), 073107 (2012).

[72] Daniel Fruchart D. Boudemagh, R. Haettel, El Kebir Hlil, A. Lacoste, L. Ortega, Nataliya Skryabina, Janusz Toboła, Pierre Wolfers, Solid State Phenomena **170**, 6 (2011); R. B. Song, T. Aizawa, and J. Q. Sun, Materials Science and Engineering: B **136** (2–3), 111 (2007).

[73] P. H. Michael Bottger, E. Flage-Larsen, O. B. Karlsen, and Terje G. Finstad, Review of Scientific Instruments **83** (2), 025101 (2012).

[74] T. C. Harman, P. J. Taylor, M. P. Walsh, and B. E. LaForge, Science (Washington, DC, U. S.) **297**, 2229 (2002).

VITA

Name: Fang Hu

Address: Department of Mechanical Engineering, TAMU 3123,
College Station, TX 77843

Email Address: hufang_gogo@tamu.edu

Education:

B.S., Mechanical Engineering, East China University of Sci. & Tech. 2007

M.S., Mechanical Engineering, Texas A&M University, 2012